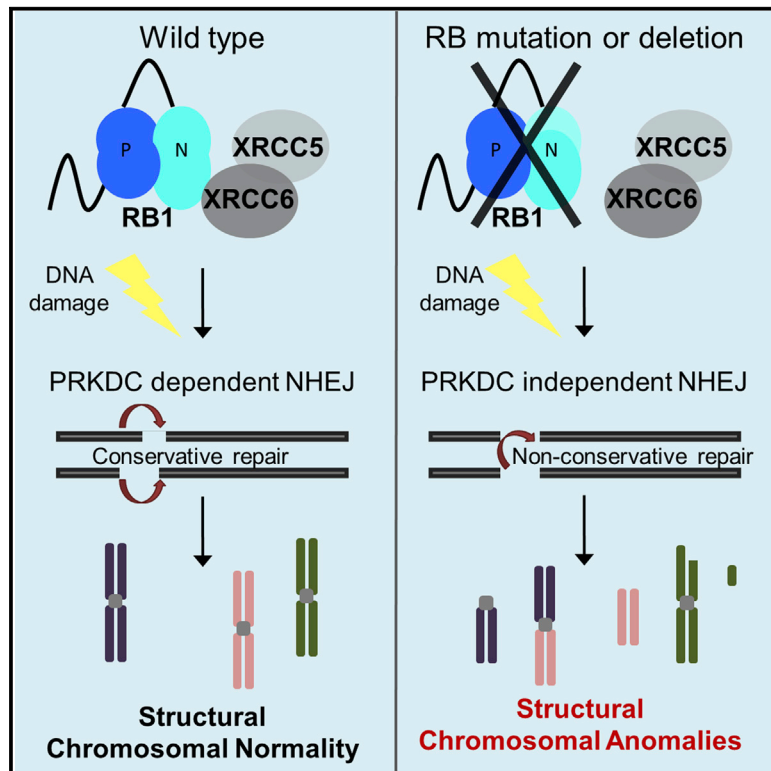


Direct Involvement of Retinoblastoma Family Proteins in DNA Repair by Non-homologous End-Joining

Graphical Abstract



Authors

Rebecca Cook,
Georgia Zoumpoulidou, ..., Paul H. Huang,
Sibylle Mittnacht

Correspondence

paul.huang@icr.ac.uk (P.H.H.),
s.mittnacht@ucl.ac.uk (S.M.)

In Brief

Loss of retinoblastoma protein (RB1) is common in various difficult-to-treat cancers. Cook et al. show that RB1 loss significantly impairs repair of DNA via non-homologous end-joining (NHEJ) and, in doing so, promotes genomic instability. These unexpected findings present opportunities for future cancer therapies that exploit this repair defect.

Highlights

- RB1 associates with XRCC5 and XRCC6, involved in DNA repair by cNHEJ
- RB family loss reduces cNHEJ and boosts repair-associated chromosomal aberrations
- cNHEJ requires RB1's N-terminal domain but is unrelated to cell-cycle control by RB1
- RB1's ability to support cNHEJ is targeted by mutation in cancer



Direct Involvement of Retinoblastoma Family Proteins in DNA Repair by Non-homologous End-Joining

Rebecca Cook,^{1,2} Georgia Zoumpoulidou,² Maciej T. Luczynski,¹ Simone Rieger,² Jayne Moquet,⁴ Victoria J. Spanswick,³ John A. Hartley,³ Kai Rothkamm,⁴ Paul H. Huang,^{1,*} and Sibylle Mittnacht^{1,2,*}

¹Division of Cancer Biology, Institute of Cancer Research, 237 Fulham Road, London SW3 6JB, UK

²Cancer Cell Signalling, UCL Cancer Institute, University College London, 72 Huntley Street, London WC1E 6DD, UK

³Cancer Research UK Drug-DNA Interactions Research Group, UCL Cancer Institute, University College London, 72 Huntley Street, London WC1E 6DD, UK

⁴Public Health England, Centre for Radiation, Chemical and Environmental Hazards, Chilton, Didcot OX11 0RQ, UK

*Correspondence: paul.huang@icr.ac.uk (P.H.H.), s.mittnacht@ucl.ac.uk (S.M.)

<http://dx.doi.org/10.1016/j.celrep.2015.02.059>

This is an open access article under the CC BY-NC-ND license (<http://creativecommons.org/licenses/by-nc-nd/3.0/>).

SUMMARY

Deficiencies in DNA double-strand break (DSB) repair lead to genetic instability, a recognized cause of cancer initiation and evolution. We report that the retinoblastoma tumor suppressor protein (RB1) is required for DNA DSB repair by canonical non-homologous end-joining (cNHEJ). Support of cNHEJ involves a mechanism independent of RB1's cell-cycle function and depends on its amino terminal domain with which it binds to NHEJ components XRCC5 and XRCC6. Cells with engineered loss of RB family function as well as cancer-derived cells with mutational RB1 loss show substantially reduced levels of cNHEJ. RB1 variants disabled for the interaction with XRCC5 and XRCC6, including a cancer-associated variant, are unable to support cNHEJ despite being able to confer cell-cycle control. Our data identify RB1 loss as a candidate driver of structural genomic instability and a causative factor for cancer somatic heterogeneity and evolution.

INTRODUCTION

DNA double-strand breaks (DSBs), where both strands of DNA are severed, pose an exceptional threat to the stability of a cell's genome. DSBs are caused by reactive adducts produced during normal metabolic reactions or following exposure to environmental genotoxins, including radiation. Inability to repair DSBs leads to DNA fragmentation and cell death. Unfaithful repair results in genetic instability (GIN) where cells may survive but chromosomes become rearranged, and genetic material mutated, duplicated, or deleted (Negrini et al., 2010).

GIN is a defining characteristic of cancer (Schmitt et al., 2012) promoting initiation and somatic evolution, in turn, linking to disease progression and therapy resistance. To identify molecular events that cause GIN is an important goal in cancer research.

DSBs can be repaired by two mechanistically distinct pathways, homologous recombination (HR) (Heyer et al., 2010) and canonical non-homologous end-joining (cNHEJ) (Lieber, 2010). HR involves single-strand resection of the damaged DNA with re-synthesis that relies on the presence of a homologous sister chromatid. cNHEJ effectively re-joins the severed DNA ends, functioning in the absence of a homologous template. Because cNHEJ has provision to trim DNA ends, it can repair breaks where DNA is chemically modified and complex damage with multiple close-by strand breaks, impeding the use of HR. Although cNHEJ has reduced accuracy compared to HR, most specifically when mending breaks that require end trimming, repair by cNHEJ is conservative as gene positioning and sequence co-linearity within chromosomes are strictly maintained and its simplicity and versatility make it the most prominent route by which DSBs are repaired in higher eukaryotes. cNHEJ also serves other roles, including VDJ recombination in immune cells and telomere maintenance (reviewed in Doksani and de Lange [2014] and Malu et al. [2012]).

Inhibition or mutational loss of cNHEJ or HR leads to use of alternative, inaccurate forms of end-joining (aNHEJ), reliant on resection that exposes serendipitous homology to adjacently positioned yet often noncontiguous chromatin that then is used as a template for repair (reviewed in Aparicio et al. [2014]). Chromosomal alterations are thus generated, including base changes, inversions, translocations, and deletions, with consequence of code alteration, gene gain, loss or deregulation, and the generation of gene fusions. Paired with mitotic checkpoint defects, such misrepair may give rise to progressive GIN.

How canonical HR and NHEJ suppress the use of aNHEJ is not clear. Answers most likely lie in the recruitment of accessory factors by the respective core repair machineries, which protect and manage regulated access to the damaged DNA. These include a diverse collection of chromatin modifying enzymes, comprising effectors of protein acetylation, methylation, and ubiquitination, as well as effectors of chromatin conformation, including the imitation switch (ISWI) chromatin remodeling complexes and the inhibitor of resection 53BP1 (reviewed in Panier and Boulton [2014] and Papamichos-Chronakis and Peterson [2013]).

The retinoblastoma protein (RB1) is an important tumor suppressor. Mutational loss of RB1 is implicated in the development of the childhood eye cancer retinoblastoma but also major cancers including breast and small cell lung cancer, sarcomas, and glioblastoma. Germline mutations in the RB1 encoding gene are associated with a highly penetrant predisposition to retinoblastoma (Lohmann, 2010) and substantially increase the lifetime risk for a spectrum of secondary cancers (Meadows et al., 2009). RB1 belongs to a family of proteins with similar molecular anatomy and related function. RB1 and its paralogs are best recognized for their role in the control of gene transcription by which they affect the cell cycle and a range of other responses, including cell differentiation, epithelial to mesenchymal transition, angiogenesis, cell migration, and metabolism (reviewed in Schaal et al. [2014]). More recently other roles of RB1 have been uncovered, fully or partially independent of its role in controlling gene transcription or the cell cycle, including the activation of apoptosis through association with the cell's mitochondria (Hilgendorf et al., 2013) and in the control of mitotic fidelity (reviewed in Manning and Dyson [2012]). The latter indicates a key contribution of RB1 in safeguarding numerical chromosomal stability and points to RB1 loss as the cause of aneuploidies observed in cancers with RB1 involvement.

Genomic analysis of retinoblastoma, a cancer that virtually always involves RB1 loss, identified widespread GIN, signified by extensive gain and loss of subchromosomal regions (reviewed in Thériault et al. [2014]), in addition to numerical chromosome abnormalities in a portion of these cancers. These observations suggest RB1 loss, in addition to numerical chromosome instability, may affect chromosome integrity, leading to GIN.

Here, we report that the RB family proteins are required for repair of DNA by cNHEJ. We show that these proteins through use of their amino-terminal domains associate with the core components XRCC5 and 6 of the cNHEJ damage recognition machinery. Our work identifies RB1 and its paralogs as critical factors in cNHEJ with roles of suppressing the use of alternative, inaccurate end-joining in cells. The work identifies RB1 loss as a plausible cause of GIN in cancers with RB1 loss.

RESULTS

Interaction between RB1^N and Components Involved in NHEJ

RB1 is built from two major folded domains, the central pocket domain, RB1^P, and the amino-terminal domain, RB1^N (Hensey et al., 1994), that between them share similarities including fold analogy and conservation of isostructural surfaces (Hassler et al., 2007). RB1^P is recognized for its ability to interact with key cellular proteins, including members of the E2 factor (E2F) family of transcription factors and proteins containing an Leu-X-Cys-X-Glu (LXCXE) linear motif (Lee et al., 1998, 2002; Xiao et al., 2003), through which RB1 confers transcriptional regulation, cell-cycle regulation, and tumor suppression (reviewed in Schaal et al. [2014]). The mode of action of RB1^N has not been mechanistically defined, although ~20% of identified frame-preserving tumor mutations reside in this domain, and deletion

results in tumor development in mice, predicting importance of this domain in tumor suppression (Goodrich, 2003).

Owing to the structural similarity of RB1^N and RB1^P, we reasoned that RB1^N, like RB1^P, may act by binding partner proteins and that identification of these will reveal the functional significance of RB1^N. To capture partner proteins, we utilized as a matrix glutathione S-transferase (GST)-tagged RB1 40-355 (RB1^N), previously employed to determine the structure of this domain (Hassler et al., 2007), together with HeLa nuclear extract, and liquid chromatography-tandem mass spectrometry (LC-MS/MS) for partner protein identification. We performed parallel experiments using purified GST tag to distinguish proteins selectively captured by RB1^N, which identified 34 proteins that selectively interacted with RB1^N (Table S1; Supplemental Experimental Procedures).

Mining for associations of these proteins with cellular processes using the Database for Annotation, Visualization and Integrated Discovery (DAVID) (Dennis et al., 2003) uncovered a number of ontologies enriched in representation by the list of interacting proteins compared to the nuclear proteome (Figure 1A), among them “DNA double-strand repair via NHEJ” and related ontologies, suggesting a connection between RB1 and NHEJ. In particular, XRCC5 (Ku80), XRCC6 (Ku70), and PRKDC (DNA-PK), required for DSB repair by cNHEJ (Lieber et al., 2003), were identified with high confidence (Table S1). Subsequent affinity capture using extract from two other cell lines, HCT116 colon and MCF-7 breast cancer cells, combined with antibody-based detection of XRCC5 and XRCC6 (Figures 1B and 1C) confirmed selective retention of these proteins by GST-RB1^N.

It has been reported that XRCC5 and XRCC6 can be contaminants associated with affinity-capture experiments (Mellacheruvu et al., 2013). To gain additional evidence for the selectivity of the observed interactions, we made use of a RB1^N variant (RB1^N^{PolyG}) with a fold-preserving alteration in the B cyclin wedge, predicted by analogy to support protein binding (Figures 1D and 1E) (Hassler et al., 2007). While XRCC6 was readily recovered from HCT116 lysate by wild-type GST-RB1^N (Figure 1C), only a minor amount of XRCC6 was recovered using GST-RB1^N^{PolyG} (Figure 1F). Identical results were obtained using RB1^N^{240-242 del}, a cancer-associated RB1 variant (Shuin et al., 1995) featuring a three amino acid deletion in the same region (Figures 1D and 1G). Together, these experiments provide strong evidence for selectivity of the interactions. They further identify a specific RB1^N region, predicted to confer protein binding (Hassler et al., 2007), as responsible for mediating the interaction with XRCC5 and XRCC6.

To document that these interactions arise with cell endogenous components, we immunoprecipitated RB1 from cells (Figure 1H). We used asynchronously growing HCT116 cells or HCT116 cells treated with the CDK4/6 selective inhibitor PD0332991, which enriches for G1 phase cells with underphosphorylated, active RB1 (Fry et al., 2004), followed by ionizing radiation (IR), to induce DSB damage. These experiments confirmed XRCC5 and XRCC6 associate with RB1 and further revealed an increased amount of XRCC5 and XRCC6 is recovered under conditions of RB1 activation and DNA damage, suggesting regulation of the interaction.

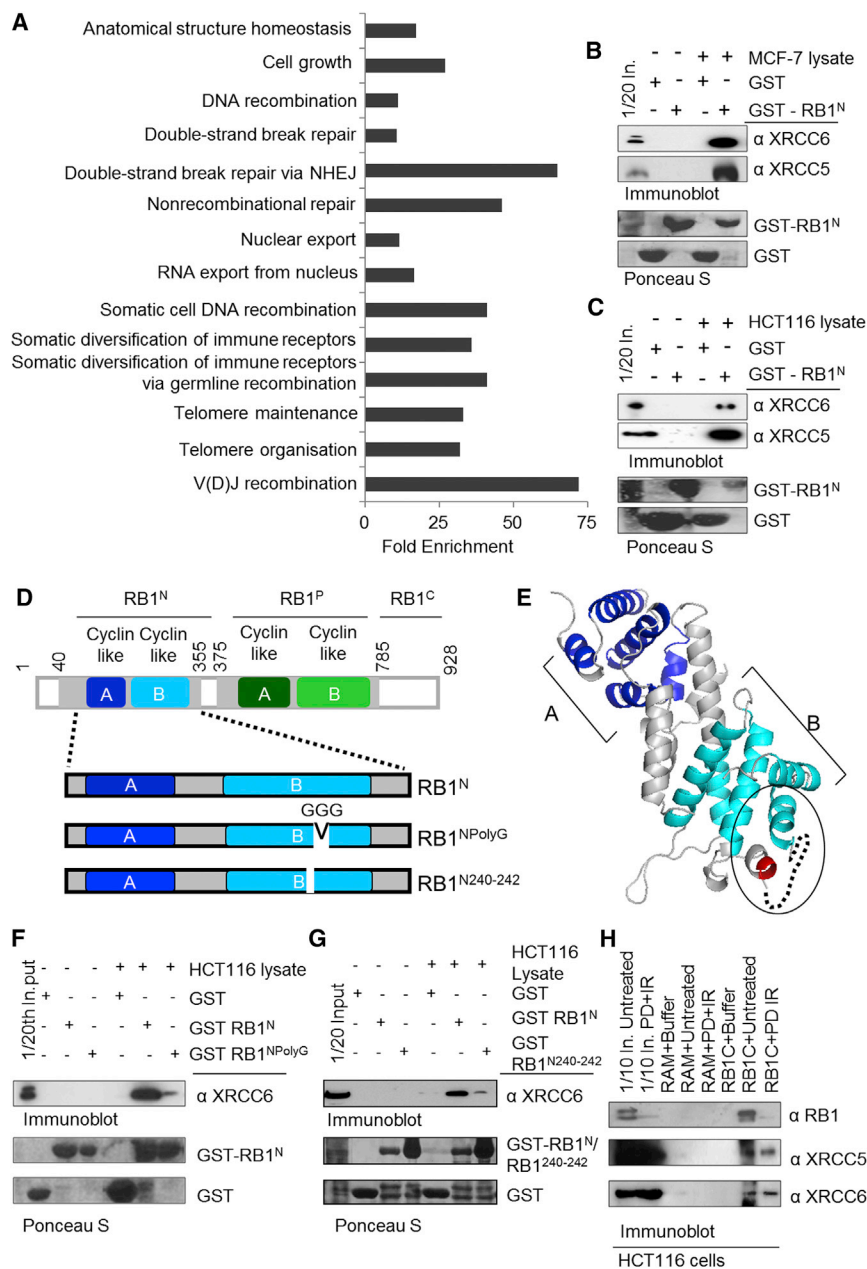


Figure 1. Interaction between RB1^N and NHEJ Proteins

(A) Graph depicting enrichment scores calculated using the DAVID gene annotation tool (biological processes). Proteins selectively captured by GST-RB1^N (amino acids 40–355) were scored against a self-generated nuclear proteome background. The ontologies shown are represented by three or more proteins with >10-fold enrichment over background.

(B and C) Affinity capture on GST RB1^N with analysis by immunoblotting. Nuclear extracts derived from MCF-7 (B) or HCT116 (C).

(D) Schematic representation of full-length RB1 (top) and the folded RB1^N (bottom). The position of the twin cyclin-like folds building the scaffold of RB1^N and RB1^P are indicated. The location of residue alterations yielding RB1^{NPolyG} and RB1^{N240–242} deletion is indicated.

(E) Ribbon diagram representation of the structure of RB1^N (adapted from Hassler et al. [2007]); the unoccupied cyclin wedge region is denoted with a circle, the location of the PolyG alteration is indicated by a dotted line, and the position of RB1^{N240–242} deletion is denoted in red.

(F) GST-affinity capture using HCT116 cell lysate with GST, RB1^N, or RB1^{NPolyG}.

(G) GST-affinity capture using HCT116 cell lysate with GST, RB1^N, or RB1^{N240–242} deletion.

(H) Co-immunoprecipitation of cell endogenous XRCC5 and XRCC6 with RB1 from HCT116. Cells were left untreated or treated with a CDK4/6 selective inhibitor of RB1 phosphorylation PD0332991 (400 nM for 18 hr) followed by irradiation at 5 Gy (IR), with extract preparation 30 min post IR. RAM, irrelevant control antiserum; RB1C, anti-RB1^C domain antiserum; In., input lysate.

complexes between XRCC6 and RB1 exist in cells, and that these were located in the cell nucleus.

A notable and statistically significant increase in both complex abundance and the number of complex-positive cells was observed when cells were pre-treated with PD0332991 followed by IR. Greater than 60% of either MCF-7 or HCT116 cells treated in this way contained six or more foci compared to

Regulation of the Interaction between XRCC6 and RB1

To further confirm RB1/XRCC5/XRCC6 complexes exist within intact cells, we employed proximity ligation (PLA), which visualizes protein interactions in fixed cells based on antibody-mediated detection of the respective interaction partners (Weibrecht et al., 2010). We probed for the interaction between RB1 and XRCC6 in both MCF-7 (Figures 2A and 2B) and HCT116 cells (Figure S1B), which were untreated or treated with PD0332991 or IR alone or in combination. To document assay selectivity, we ablated RB1 using small interfering RNA (siRNA) (Figure 2D; Figures S1A, S1D, and S1E) or omitted one or both primary antibodies (Figures S1F and S1G). These experiments confirmed

20%–25% treated with PD0332991 or IR alone, and <15% of untreated cells (Figures 2B, S1F, and S1G; statistics in Table S2). Immunoblotting confirmed loss of RB1 phosphorylation in PD0332991-treated cells (Figure 2C). Notably, differences in interaction seen by PLA were not paralleled by differences in the levels of XRCC5, XRCC6, or RB1 in the cells, excluding protein abundance changes as the cause for the increase in interactions. We also assessed MCF-7 and HCT116 cells enriched for mid-S or G2/M phase alongside cells enriched for G1 using PD0332991. Flow cytometry confirmed appropriate cell-cycle distributions (Figures 2G and S2E). We observed absence of foci in the vast majority of mid-S and G2/M-enriched cells but

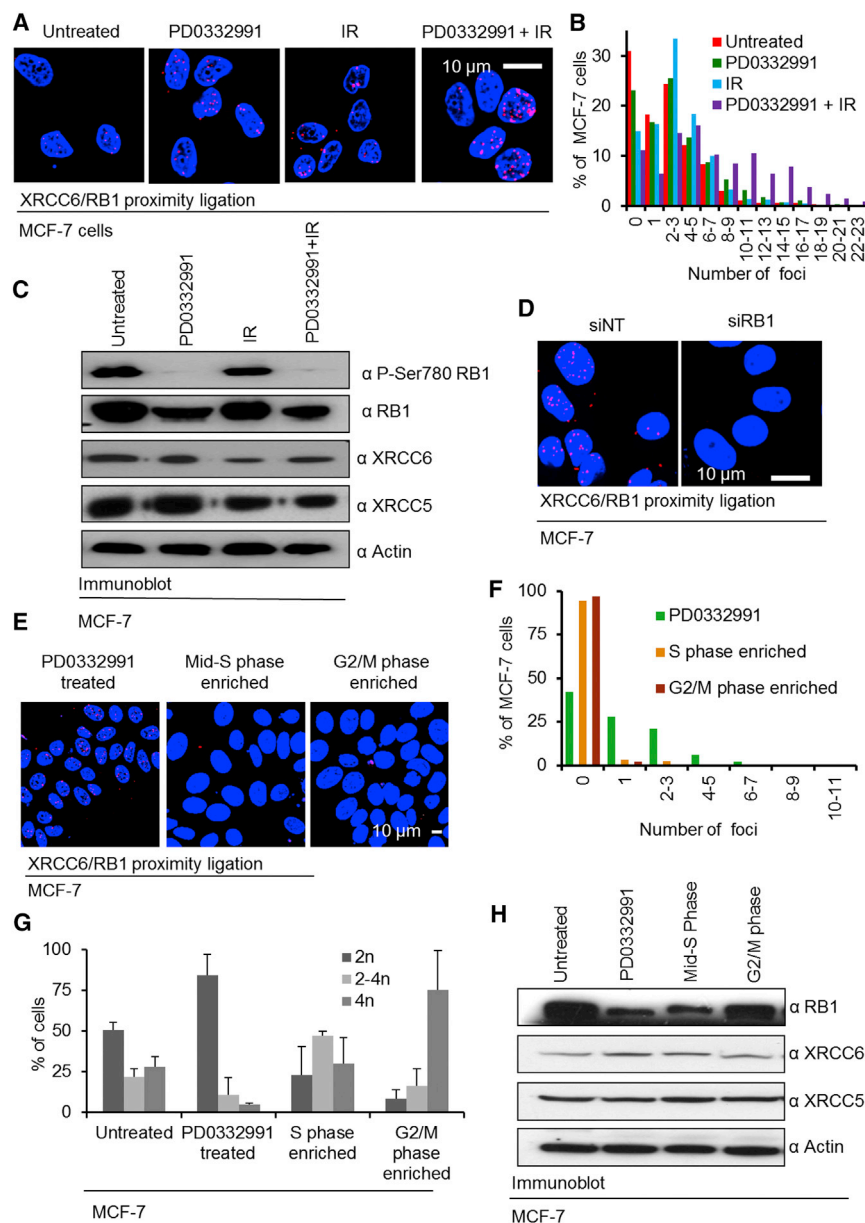


Figure 2. Regulation of the Interaction between XRCC6 and RB1 in Cells

(A) PLA probing for XRCC6/RB1 complex in MCF-7 cells. Cells were left untreated or treated with the PD0332991 (400 nM for 18 hr), IR (5 Gy) or PD0332991 (400 nM for 18 hr) followed by IR (5 Gy). Cells were analyzed 30 min post IR. Nuclei visualized with Hoechst 33258. Parallel staining in the absence of primary or secondary antibodies shown in Figure S2A. Identical experiments using HCT116 shown in Figure S1B.

(B) Automated quantification of PLA foci. Data represent counts for a minimum of 100 cells per condition from $n = 3$ biological repeats. The percentage of cells for each range of interactions is shown. For statistical assessment of results, see Table S2.

(C) Immunoblotting analysis of P-Ser780 RB1, serving as a biomarker for CDK4/6 activity. XRCC5 and XRCC6 and RB1 total protein levels were also assessed. Actin levels are shown as loading controls.

(D) PLA probing for XRCC6/RB1 complex in MCF-7 cells treated with non-targeting (siNT) or RB1 targeting siRNA. Cells were treated with PD0332991 followed by 5 Gy IR as described for (A). For parallel anti-RB1 staining, see Figure S1A. Identical experiments using HCT116 shown in Figures S1D and S1E.

(E) Detection of RB1/XRCC6 complex in cell-cycle-phase-enriched cells. Cells were enriched for the various cell-cycle phases as depicted in Figure S2A. XRCC6/RB1 complexes were detected using PLA. Related data for HCT116 are shown in Figure S2.

(F) Automated quantification of foci number. Cumulative data for $n = 3$ biological replicates are shown. Data represent evaluation of a minimum of 100 independent cells. Quantification was performed as for (B).

(G) Cell-cycle profiles of the cells analyzed in (E), determined by propidium iodide staining and flow cytometry. Error bars represent \pm SD for $n = 3$ biological replicates.

(H) Immunoblotting analysis depicting protein levels of RB1, XRCC5, and XRCC6 in cells enriched for the various cell-cycle phases. Actin levels are shown as loading controls.

presence of foci in many of the G1 enriched cells (Figures 2E–2H and S2; statistics in Table S3). Likewise, these differences were not paralleled by altered abundance of RB1, XRCC5, or XRCC6 (Figures 2H and S2C). Together, these results provide additional evidence for complex formation between the NHEJ components and RB1, which appears to be promoted by RB1 activation and DSBs, in line with our earlier observations using RB1 immunoprecipitation.

RB Family Proteins Promote PRKDC-Dependent NHEJ

Since different methodologies confirmed the interaction of RB1 with components involved in cNHEJ, we assessed whether RB1 affects NHEJ activity in cells. To do so, we used a reporter (Bennardo et al., 2008) (Figure 3A) in which a removable puromy-

cin-resistance gene is inserted between the GFP reading frame and its promoter. I-SceI expression in cells induces removal of the insertion, leaving a DSB that when repaired by NHEJ leads to GFP expression (GFP^{*}), allowing quantification of repair proficiency by flow cytometry. We quantified NHEJ proficiency in HCT116 cells in which siRNA was used to deplete RB1 either alone or together with its paralogs RBL1/p107 and RBL2/p130, known to act redundantly with RB1 in many cell types (Henley and Dick, 2012). To identify cells with reporter uptake, we co-transfected plasmid encoding red fluorescent protein (DsRed). RB1 depletion led to a significant reduction in NHEJ proficiency (Figures 3B and 3C) that was further augmented by co-depletion of RBL1 and RBL2 (Figure 3C), confirming a redundant role of the RB paralogs in NHEJ in HCT116. Cell-cycle analysis performed

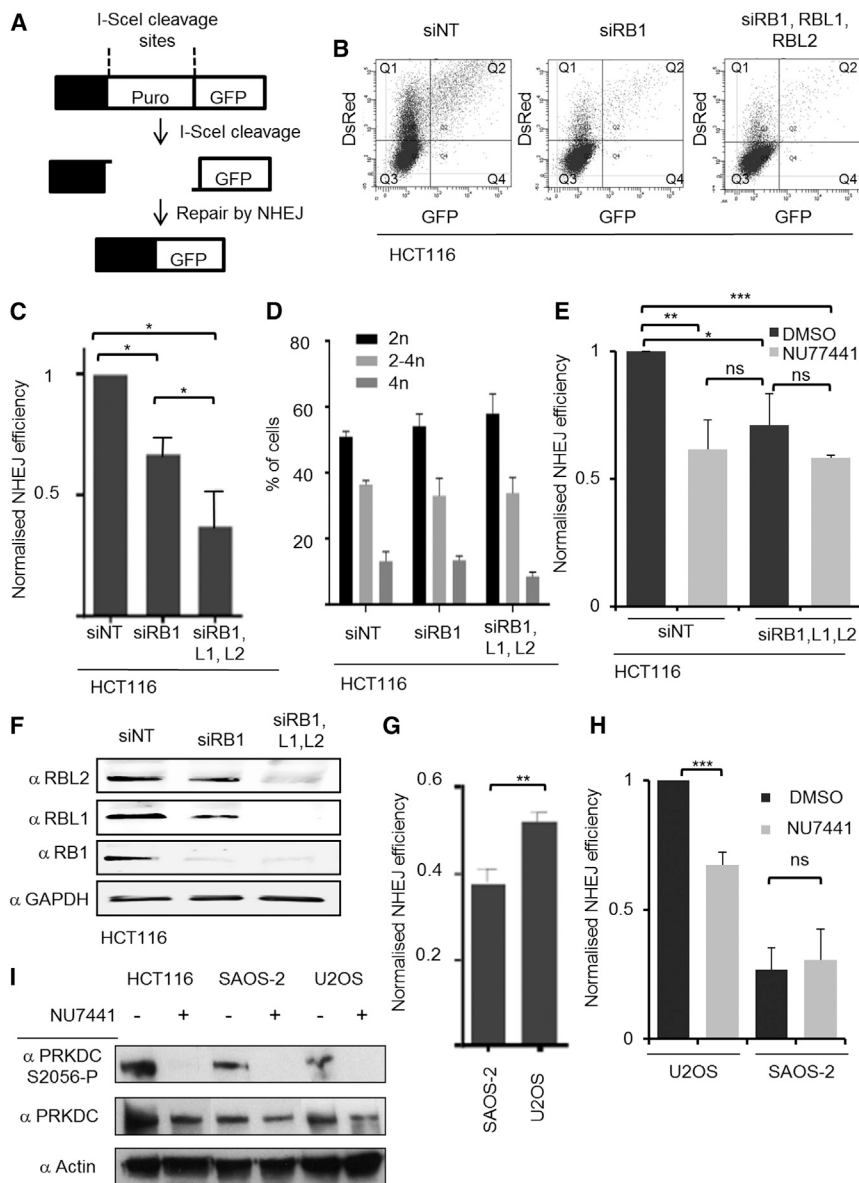


Figure 3. RB Family Proteins Promote PRKDC-Dependent NHEJ

(A and B) Reporter-based quantification of NHEJ repair. Cells were transfected with NHEJ reporter and I-SceI encoding plasmid to introduce DSBs, with repair by NHEJ yielding GFP-positive cells (A). DsRed was used to identify transfected cells. Assays were quantified using flow cytometry. Representative raw images for HCT116 cells treated with siRNA targeting RB1 or RB1, RBL1, and RBL2, or a non-targeting control (siNT) are shown (B) NHEJ repair proficiency is determined by calculating the ratio of GFP-positive (Q2) versus DsRed-positive cell (Q1 + Q2).

(C) Graph depicting repair proficiency in NHEJ reporter-transfected cells. Cells were treated as for (B). NHEJ repair proficiency for cells transfected with siNT was set to 1. Binding of XRCC5 by RBL1 and RBL2 shown in Figure S3.

(D) Cell-cycle profiles for DsRed-positive cells from (C).

(E) Effect of PRKDC inhibition on reporter repair proficiency. HCT116 cells were treated and evaluated as for (C). DMSO or the PRKDC inhibitor NU7441 (5 μ M) was added for the duration of the experiment.

(F) Immunodetection documenting RB1 and RB protein family loss in HCT116. HCT116 transfected with siRNA as in (C)–(E). Lysates probed using antibodies as indicated.

(G) NHEJ proficiency in SAOS-2 (RB1-negative) and U2OS (RB1-positive) cells using transient NHEJ reporter transfection as for (C) and (D).

(H) Effect of PRKDC inhibition on NHEJ proficiency. SAOS-2 and U2OS cells with integrated NHEJ reporter were used. Lines were transfected with I-SceI and DsRed plasmids and treated with DMSO or NU7441 as for (E). For all experiments, the average for $n = 3$ biological replicates is depicted; error bars \pm SD. * $p < 0.05$, ** $p < 0.01$, *** $p < 0.001$ using a paired Student's t test.

(I) Immunodetection of PRKDC-Ser2056 phosphorylation status. Autophosphorylation of PRKDC-Ser2056 signifies PRKDC activity. Cells were treated with 5 μ M NU7441 for 24 hr prior to 5 Gy IR. 2 hr post IR, the cells were harvested into SDS protein loading buffer. Actin and total PRKDC levels are shown as loading controls.

in parallel for DsRed⁺ cells of the various treatment groups detected no statistically significant differences, indicating that functional RB loss in these cells, within the time frame and manipulations undertaken, does not cause overt cell-cycle differences (Figure 3D). Hence, cell-cycle differences are not the cause of the difference in reporter repair proficiency that we detect.

Since our functional analysis indicates RBL1 and/or RBL2 act redundantly to RB1 in NHEJ, we sought to address whether these RB1 paralogs interact with NHEJ components, as observed for RB1. Using GST-fused fragments of RBL1 and RBL2 homologous to RB1^N together with HCT116 nuclear extract, we performed affinity-capture experiments as for Figure 1, with control reactions containing GST-RB1^N or unfused GST (Figure S3). These experiments clearly document selective

capture of XRCC5 by RBL1 and RBL2 arising with comparable efficacy to that seen for RB1 (Figure S3B).

The NHEJ reporter used measures cNHEJ as well as some portion of aNHEJ that is independent of PRKDC (Chiruvella et al., 2013). To distinguish between these different forms of NHEJ repair, we treated reporter-transfected cells with NU7441, a PRKDC inhibitor, which prevents cNHEJ (Zhao et al., 2006). We found that NU7441 reduced NHEJ reporter activity significantly ($p < 0.01$) in control cells but not in cells with ablation of RB family proteins (Figure 3E). This data provide strong evidence that repair reduction following RB family protein depletion results from loss of cNHEJ with the detected residual reporter activity arising from PRKDC-independent repair.

To probe whether cNHEJ is affected in cancers with mutational RB1 loss, we assessed reporter repair in SAOS-2 osteosarcoma

cells, which carry an inactivating mutation in RB1 (Hellwinkel et al., 2005) and U2OS osteosarcoma cells, which have wild-type RB1. Using transient reporter transfections, SAOS-2 cells displayed a significantly lower level of NHEJ capacity (Figure 3G) compared to U2OS cells. We further used SAOS-2 and U2OS lines with stable chromosomal integration of the NHEJ reporter, assessing their respective propensity to undertake PRKDC-dependent, NU7441-sensitive repair. NU7441 did not affect repair proficiency in SAOS-2 cells but significantly reduced repair proficiency in the U2OS cells (Figure 3H). These experiments provide direct evidence for diminished use of cNHEJ in RB1 mutated cancer cells. They in addition confirm repair loss is observable in chromosomally integrated, chromatinized settings. Immunoblotting for PRKDC autophosphorylation (Ser2056) indicated that NU7441 achieved PRKDC inhibition in HCT116, SAOS-2, and U2OS cells (Figure 3I). This analysis further reveals activation of PRKDC occurs in SAOS-2, indicating that PRKDC activation, an early step of cNHEJ repair, arises independently of RB1 function.

The Role of RB1^N in NHEJ

To test whether re-expression of RB1 reinstates the capacity of RB1-negative cells to perform cNHEJ, we transfected plasmid encoding human RB1 (Chew et al., 1998) alongside the NHEJ reporter into SAOS-2 cells. We also transfected these cells with plasmid encoding the PolyG alteration shown in our earlier experiments (see Figures 1D and 1E) to disable the interaction with XRCC6. Expression of RB1 significantly increased NHEJ competency compared to vector transfection. In contrast, RB1^{PolyG} was unable to increase NHEJ proficiency (Figure 4A). Furthermore, expression of RB1 but not expression of RB1^{PolyG} restored sensitivity of repair to NU7741, supporting that RB1 but not RB1^{PolyG} reinstates use of cNHEJ in the transfected cells. Parallel immunoblotting revealed equal expression of RB1 and RB1^{PolyG} (Figure 4C). Identical results also were obtained with the XRCC6 binding-defective cancer-associated variant, RB1^{240–242 del} (Figure S4), which like RB1^{PolyG} was unable to support NHEJ despite appropriate expression. RB1 strongly inhibited cell-cycle progression in the transfected SAOS-2 cells, promoting their accumulation and stable arrest in G1 (Figure 4B). This is an expected outcome for RB1-negative cancer cells, where transformation associated hyperactivation of the INK4/ARF locus prevents cell-cycle-dependent RB1 inactivation, and contrasts to cancer and primary cells containing wild-type (WT) RB1 expression that usually are competent to inactivate RB1 (Hinds et al., 1992). Significantly, cell-cycle arrest was seen also where RB1^{PolyG} (Figure 4B) and RB1^{240–242 del} (Figure S4B) were used, with no statistically significant difference detectable compared with RB1. These results provide direct evidence that enablement of cNHEJ by RB1 is not an attribute, or consequence, of G1 cell-cycle arrest, which can be actioned by NHEJ-competent WT RB1 and the NHEJ-incompetent variants alike, but involves a mechanism distinct and genetically separable from that involved in cell-cycle control. This conclusion is supported further by experiments run under conditions that did not involve DNA damage reporter co-expression, revealing identical potency of RB1, RB1^{PolyG}, and RB1^{240–242 del} to support G1 cell-cycle arrest and E2F regulation

and to suppress colony outgrowth of SAOS-2 cells (Figures 4D–4H and S4D–S4H).

The described observations in SAOS-2 were also corroborated by experiments using mouse embryo fibroblasts (MEFs) with disruption of RB1, RBL1, and RBL2 (TKOs) (Dannenberg et al., 2000). Expression of RB1 significantly increased NHEJ competency, while RB1^{PolyG}, despite adequate expression, did not (Figures 4I and 4L). In these cells, no significant impact on cell-cycle distribution or the ability to progress through the cell cycle to G2 was detected upon expression of either wild-type RB1 or RB1^{PolyG}, in keeping with the ability of these primary cells to undertake cell-cycle-dependent RB1 inactivation, providing further emphasis that the differential support of NHEJ is not explained by differential effects of the two RB1 forms on the cell cycle and is not relying on dominant cell-cycle arrest instilled by RB1 (Figure 4K). In summary, these results provide strong evidence for a role of RB1 in supporting cNHEJ. They further document a mechanism of action distinct from RB1's function of controlling cell-cycle progression and reveal selective loss of ability to support NHEJ in RB1 variants defective for XRCC5 and XRCC6 binding, including a naturally occurring cancer-associated variant.

RB Family Protein Loss Impairs DNA Damage Clearance

Loss of cNHEJ in cells leads to use of alternative, slower forms of repair, resulting in reduced speed by which DSBs are resolved (Kinashi et al., 2011; Vandersickel et al., 2010). We therefore determined whether repair speed was reduced by RB1 loss using TKO MEFs as well as congenic MEFs with disruption in RB1 (RB1^{-/-}) (Jacks et al., 1992), measuring loss of γ H2AX foci as a surrogate for the DSBs resolution (Kuo and Yang, 2008) (Figure 5A).

Automated high-content image analysis (Figures 5B–5D) revealed a delay in γ H2AX signal loss detectable within 2 hr post IR, indicative of reduced repair speed in both these genetic backgrounds within a time frame comparable to that reported for cells with XRCC5 and XRCC6 loss (Kinashi et al., 2011; Vandersickel et al., 2010). Furthermore, repair delay was exaggerated in TKO compared to RB1^{-/-} MEFs, consistent with our previous observations documenting exacerbated repair loss in HCT116 with combined loss of RB paralogs (Figure 3). Quantification of cells with residual damage confirmed significantly reduced γ H2AX clearance in MEFs with RB1 or RB family loss (Figure 5C). Similar levels of γ H2AX fluorescence were observed early (15 min) after exposure to IR in all MEF lines, indicating that differences in γ H2AX signals at later time points do not reflect a difference in the amount of initial damage (Figure 5C).

The speed by which DSBs are repaired is dependent on cell-cycle position (Chapman et al., 2012). To address whether the differences in repair proficiency observed could be due to differences in the cell-cycle distribution between the different MEF lines, we measured the DNA content by integrating the intensity of the Hoechst DNA stain in the same cells that were quantified for γ H2AX intensity. Histograms generated from these measurements revealed typical cell-cycle profiles (Figure S5), but no significant differences in the overall cell-cycle distributions between backgrounds in any of the three experiments as assessed by Wilcoxon rank-sum testing. Similarly, t testing following gating for

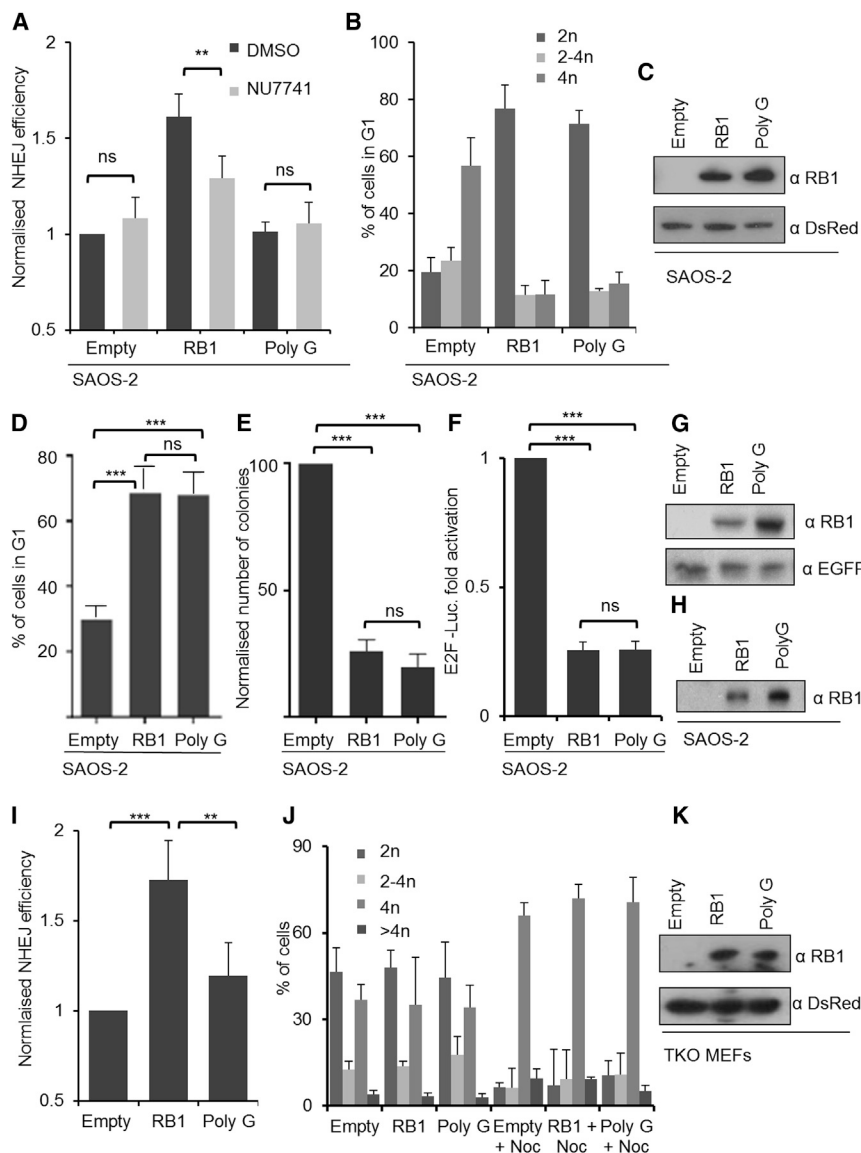


Figure 4. The Role of RB1^N in NHEJ

(A) NHEJ proficiency in SAOS-2 cells expressing RB1 or RB1^{PolyG} variant and response to NU7741 treatment. Data evaluation was as for Figure 3. Related data for RB1^{240–242} deletion are shown in Figure S4.

(B) Cell-cycle profiles for cells transfected alongside cells from (A). Nocodazole was added 16 hr before harvest to quantify stable G1 arrest.

(C) Immunodetection of RB1 and RB1^{PolyG} in SAOS-2 from (A); loading was normalized for co-transfected DsRed expression plasmid.

(D) Proficiency of RB1^{PolyG} to inhibit cell-cycle progression in SAOS-2. Graph depicts percentage of cells with stable G1 arrest, assessed as in (B). SAOS-2 cells transfected with empty vector, RB1, or Poly G expression vector. Related data for RB1^{240–242} deletion are shown in Figure S4.

(E) Proficiency of RB1^{PolyG} to inhibit colony formation. SAOS-2 transfected with empty RB1 or RB1^{PolyG} encoding vector in combination with vector for puromycin resistance and scored for outgrowth of puromycin resistant colonies. Co-transfected β-galactosidase was used to normalize data to transfection efficacy. Related data for RB1^{240–242} deletion are shown in Figure S4.

(F) Proficiency of RB1^{PolyG} to regulate E2F activity. E2F reporter activity in SAOS-2 cells. Cells were transfected with RB1, RB1^{PolyG}, or empty expression vector together with E2F promoter luciferase reporter. Co-transfected β-galactosidase was used to normalize data to transfection efficacy. Related data for RB1^{240–242} deletion are shown in Figure S4.

(G) Immunodetection of RB1 and RB1^{PolyG} in SAOS-2 used in (D) and (E). Loading was normalized using co-transfected EGFP expression plasmid.

(H) Immunodetection of RB1 and RB1^{PolyG} in SAOS-2 used in (F). Loading was normalized to β-galactosidase activity.

For all experiments the average for n = 3 biological replicates is depicted; error bars ± SD. *p < 0.05, **p < 0.01, ***p < 0.001 using a paired Student's t test.

(I) NHEJ proficiency in TKO MEFs transfected with empty vector or vector expressing RB1 or RB1^{PolyG} variant. Data evaluation was as for (A). Values for MEFs transfected with empty vector were set to 1.

(J) Cell-cycle profiles of reporter transfected TKO MEFs, analyzed as for Figure 4I. Profiles with or without secondary nocodazole block are shown. Data represent transfected cell fractions deduced using DsRed for gating.

(K) Immunodetection of RB1 and RB1^{PolyG} in MEFs from (I); loading was normalized for co-transfected DsRed expression plasmid.

cells with <2n, 2n, >2–4n, and >4n DNA content (Figure S5) revealed no statistically significant difference for any of these categories at any of the observed time points, ruling out overt cell-cycle variations as an explanation for the differences in DSB clearance observed.

Effect of RB Protein Loss in the Maintenance of Chromosomal Integrity

To obtain direct evidence that RB protein loss impairs DNA repair and assess whether RB protein loss adversely affects chromosomal integrity as expected for cells with cNHEJ defect (Iliakis et al., 2004), we determined chromatin repair and chromosomal radiation sensitivity using comet analysis and metaphase

spreads (Figure 6). Comet analysis detected a significant increase in cells with excess unligated chromatin, detectable as late as 8 hr after irradiation in cells with RB family loss. Similar results were obtained for TKO MEFs compared to WT MEF and HCT116 in which RB family proteins were depleted using siRNA compared to either mock-treated HCT116 or HCT116 treated with a nontargeting oligonucleotide (Figure 6; for raw data, see Figure S6). No significant difference was observed in the amount or distribution of DNA damage immediately after irradiation, indicating defective DNA repair as opposed to increased damage susceptibility in cells with RB family loss. We also assessed radiation-induced excess first division chromosomal aberrations, initially using HCT116 cells with siRNA-mediated RB family

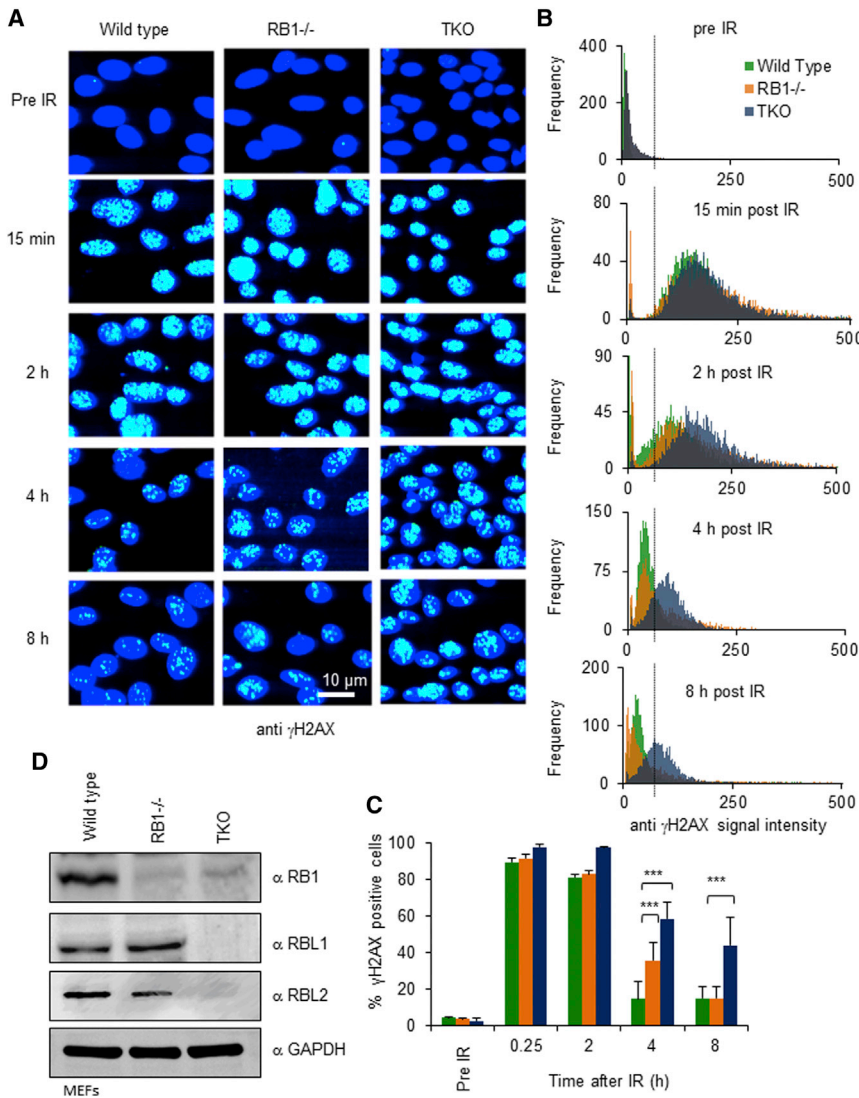


Figure 5. RB Family Protein Loss Impairs DNA Damage Clearance

(A) DSB clearance in cells with compromised RB1 function. Wild-type, RB1^{-/-}, or RB1/RBL1/RBL2-null (TKOs) mouse embryonic fibroblasts (MEFs) were exposed to IR of 5 Gy. Prevalence of damage at the indicated times was detected by immunofluorescence staining for γ H2AX (green); nuclei were visualized with Hoechst 33258 (blue). Raw images recorded using a high-content imaging platform are shown. Scale bar represents 10 μ m. (B and C) Automated quantitative assessment of damage clearance. γ H2AX staining intensity (iSig) was determined for all cells from 30 independent eye fields. (B) Integrated H2AX signal distribution for cells from one representative experiment. The dotted line shows the gating position for cells with above baseline anti- γ H2AX fluorescence. DNA content analysis for the same samples shown in Figure S5. (C) Percentage of cells with residual damage determined by gating (dotted line) for cells with above baseline anti- γ H2AX fluorescence at each time point. Error bars represent \pm SD for n = 3 biological replicates. *p < 0.05, **p < 0.01, ***p < 0.001 using a paired Student's t test comparing RB1^{-/-} or TKOs to wild-type cells. (D) Immunodetection documenting RB protein family loss in MEFs. Lysate from MEFs used for (A)–(C) were probed using antibodies as indicated.

family protein loss is associated with canonical features observed in cells with defective cNHEJ, including loss of PRKDC-dependent damage repair, delayed damage clearance, and excess genotoxin-induced structural chromosomal aberrations.

Loss of cNHEJ promotes chromosomal rearrangements presumed to arise from increased use of error-prone aNHEJ (Rothkamm et al., 2003). Our experiments documenting delayed repair kinetics and

loss. We observed a significant increase in the frequency of chromosomal aberrations compared to mock-transfected cells, comprised of increased chromosome-type aberrations and surplus chromatid breaks (Table S4). Identical results were obtained when we treated these same cells with siRNA targeting DNA ligase 4 (LIG4), involved in DNA strand ligation in cNHEJ. We also probed for loss of chromosomal integrity in irradiated TKO MEFs, revealing a consistent and significant increase of chromosome-type aberrations compared to congenic wild-type MEFs (Figure S6; Table S4). Together these results strongly support the notion that loss of RB function significantly impairs cellular DSB repair and significantly increases the incidence of structural chromosomal aberrations and chromosomal instability.

DISCUSSION

We here document a thus-far-unrecognized role of the RB family in supporting DNA repair by cNHEJ. We show that RB

excess same cycle chromosomal aberrations in cells with RB family protein loss is consistent with this notion. We note that the excess of chromosomal aberrations is more pronounced and diverse in transformed HCT116 cells compared to primary MEFs. Differences in type and level of chromosomal aberrations between primary and transformed cells with cNHEJ loss have been noted previously (Burma et al., 2006) and may be explained by loss of DNA integrity surveillance in cancers cells, permitting survival and cell-cycle progression despite reduced repair.

A substantial body of recent work has documented loss of mitotic fidelity in cellular models with RB1 loss (Manning and Dyson, 2012) and loss of mitotic fidelity is well suited to explain the development of chromosomal aneuploidy seen in retinoblastoma tumors. However, loss of mitotic fidelity cannot explain the spectrum of GIN seen in retinoblastoma. Genomic profiling of malignant retinoblastoma compared to premalignant retinoma lesions suggests complex GIN is associated with malignant progression in this disease (Dimaras et al., 2008; Sampieri et al.,

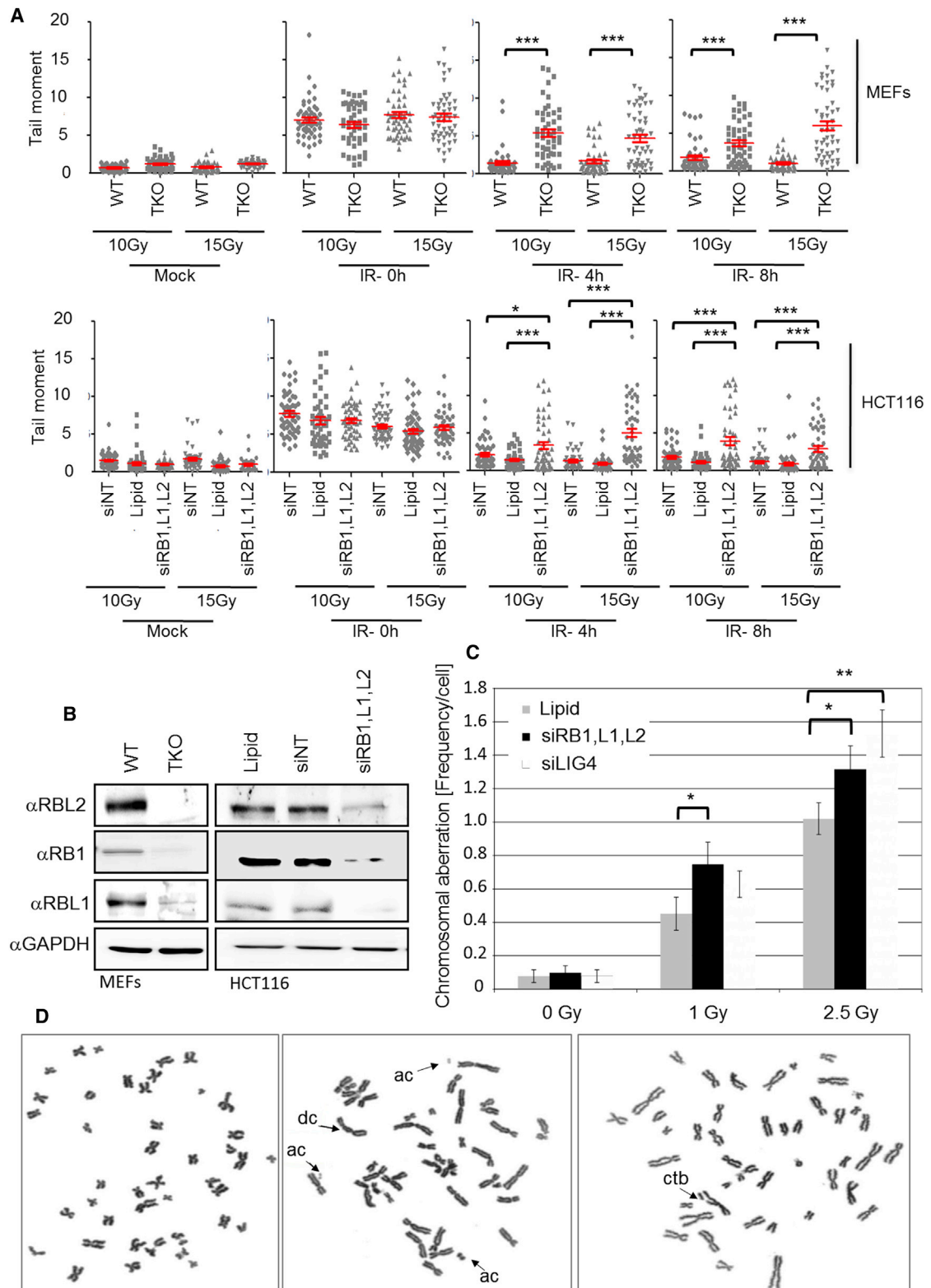


Figure 6. RB Family Loss Impairs Break Repair and Increases Radiation Induced Chromosomal Aberration

(A) Analysis of DNA strand break induction and repair by Comet assay. Data for wild-type and RB family defective (TKO) MEFs and data for HCT116 colorectal cancer cells transfected with siRNA targeting RB family proteins RB1, RBL1, and RBL2, a non-targeting control (NT), or in the absence of oligonucleotide are

(legend continued on next page)

2008) and GIN, comprising extensive copy-number changes and rearrangements, is prominent in late onset, sporadic disease, with presence in early onset, familial cases, although to a lesser degree (Thériault et al., 2014). These observations identify GIN as a relevant, albeit facultative event in retinoblastoma progression consistent with a concept whereby defective repair following from RB1 loss combines with stochastic factors, including environmental genotoxin exposure and checkpoint loss, that cooperate to unleash GIN in this disease. Significantly, recent work documented excess micronuclei formation, indicative of excess acentric chromosome fragments, in primary murine osteoblasts with RB1 loss, exacerbated by IR (Gonzalez-Vasconcellos et al., 2013), which is in agreement with our observations of excess genetic aberration in cells with loss of RB function. Importantly, evidence of excess chromosomal aberrations was apparent in cells with heterozygous loss of RB1, inferring systemic repair defects may manifest in individuals with constitutional RB1 mutation where heterozygous defects are present in somatic tissue. Defective DSB repair with excess genotoxin-driven genetic aberration documented here and in Gonzalez-Vasconcellos et al. (2013) may explain the recognized risk for secondary cancers in such patients following external beam radiotherapy and genotoxic chemotherapy, for which a mechanistic justification has thus far been lacking (Kleinerman et al., 2012; Wong et al., 2014).

Our data allow us to draw several mechanistic conclusions pertaining to the contribution of RB1 to cNHEJ. We identify two different fold-preserving variants affecting RB1^N that are defective for the interaction with XRCC6. Significantly, we document that these RB1 variants are unable to support NHEJ in primary MEFs with RB family loss and in cancer-derived SAOS-2 osteosarcoma cells with spontaneous inactivation of RB1. Together these results provide strong support that the physical interaction with cNHEJ proteins underlies the mechanism through which RB1 affects this form of repair. Importantly, RB1 variants defective in supporting NHEJ were capable of blocking cell-cycle progression and E2F transcriptional activation as effectively as WT RB1, providing strong support that neither loss of cell-cycle inhibition nor loss of E2F regulation provide a mechanistic explanation for the contribution of RB proteins in NHEJ that we describe. A recent report demonstrates stimulation of HR following enforced expression of RB1 in a RB1-mutated, retinoblastoma-derived cell line, which could suggest a potentially broader role of RB1 in DSB repair (Yang et al., 2013). Whether RB1 has a direct critical role in HR or whether cell-cycle changes seen to arise in the cells following RB1 expression indirectly affected repair pathway choice is not known. HR components were not identified in the mass spec-

trometry approach we used suggesting the mechanistic contribution of RB1 to NHEJ and HR is distinct. As noted DSB repair involves extensive chromatin modification. RB1 and its paralogs can facilitate chromatin modification through recruitment of chromatin modifiers that mostly interact with RB1^P and the RB1 carboxyterminal region (reviewed in Manning and Dyson [2012] and Talluri and Dick [2012]). Intriguingly, several of these modifiers are known to be involved in cNHEJ, including the ISWI remodeling machine (Aydin et al., 2014), the HDAC1 and 2 histone deacetylases (Miller et al., 2010), the SUV4 histone methyl transferase (Tuzon et al., 2014), and the inhibitor of resection 53BP1 (Carr et al., 2014). A proposition for a mechanism of action how RB family proteins support cNHEJ could be that they, by way of interaction with the damage recognition complex, recruit these chromatin modifiers to the site of DNA repair.

A considerable body of evidence supports the view that cNHEJ is active and has major roles during G1 and early S (Branzei and Foiani, 2008), the cell-cycle phases where RB family proteins are naturally active or are known to be activated by DNA damage-associated inhibition of the CDK4, 6, and 2 cyclin-dependent kinases. Recent work has shown that cNHEJ is also used in G2 (Kakarougkas and Jeggo, 2014), where RB proteins are not known to be active. Our quantitative data based on monitoring reporter repair argue the contribution of RB family proteins is considerable, with little PRKDC-dependent repair activity observed in cells with RB loss. However, G2 phase cells are naturally underrepresented in actively proliferating cell populations. Hence, the quantitative contribution of G2 cells to the total repair activity within the population is expected to be small and may remain underreported by the reporter-based assessment used here.

NHEJ plays a key role in VDJ recombination, and mutations in components of cNHEJ, including PRKDC and Artemis, result in severe combined immunodeficiency (SCID) affecting B and T cell maturation in humans and mice (Woodbine et al., 2014). While there is evidence that mechanistic differences between DSB repair and VDJ exist (Malu et al., 2012), it is possible that RB1 loss alone or together with its paralogs affects VDJ recombination in addition to DSB repair. Homozygous loss of RB1 is embryonic lethal in mice (Jacks et al., 1992) and presumably in human. RB1 loss arises in individuals with somatic or germline heterozygous mutations upon subsequent loss of the wild-type allele through secondary mutation or mitotic nondisjunction. Given the rarity of these events, it would not be expected that VDJ deficiency and associated pathologies are observable, or clinically relevant, in this context. However, several studies have assessed the effect of engineered RB1 and RB family

shown. Cells were treated with either 10 or 15 Gy and harvested for analysis at the indicated time. Data shown are derived from two independently processed technical replicates. 25 cells per replicate were analyzed.

(B) Immunodetection documenting RB protein family loss in MEFs and HCT116. Lysates were prepared from MEFs and HCT116 used for (A), (C), (D), and Figure S6 and probed using antibodies as indicated.

(C) Chromosome aberration analysis. HCT116 treated with siRNA as for (A) were irradiated with the dose indicated. Cells were processed for analysis 16 hr post IR. Colcemid was added for the final 10 hr. Table S4 provides full numerical details of all analyses. Errors represent SEM. Related analysis of wild-type and TKO MEFs shown in Figure S6.

(D) Examples of Giemsa-stained metaphases, documenting aberrations detected in HCT116. Examples of Giemsa-stained metaphases from HCT116 cells documenting exemplary aberration scored. Aberrations denoted by arrows; dc, dicentric; ac, excess acentric fragment; ctb, chromatid break. Error shown represents SEM. **p* < 0.05, ***p* < 0.01, ****p* < 0.001 using an unpaired heteroscedastic Student's *t* test.

deletion on the hematopoietic system in the mouse (Daria et al., 2008; Viatour et al., 2008; Walkley and Orkin, 2006). Although these studies did not explicitly address whether VDJ recombination is lost, phenotypes consistent with such loss were observed. Two independent studies examining RB1 deletion note a considerable decrease in B cells with IGG/IGM rearrangement, although the number of B cells precursors with un-rearrange IGG/IGM was not unaltered (Daria et al., 2008; Walkley and Orkin, 2006). No effect on T cell maturation was observed, which might be explained by redundant functioning of RB family proteins in this lineage. Radical loss of common lymphoid precursors was observed following combined deletion of the RB family (Viatour et al., 2008), indicating additional and profound early lineage reliance on RB family proteins at a stage predating T cell differentiation and VDJ recombination, precluding conclusions as to the role of the RB family in VDJ recombination in this lineage.

Our experiments document that the role of RB1 in cNHEJ involves the RB1^N domain. Although a role of RB1^N in tumor suppression had been anticipated (Blanquet et al., 1995; Lee et al., 1992; Lohmann et al., 1997), a mechanistic basis of how defects in this region contribute to cancer development has remained elusive. This work now demonstrates a defined functional role of this domain. The involvement of RB1^N in supporting cNHEJ provides a plausible mechanistic explanation for tumorigenicity associated with mutations in this region.

Our results have important conceptual implications in that they identify RB family proteins as cofactors supporting cNHEJ and predict impairment of this repair pathway in RB1-negative cancers with consequence of structural chromosomal instability that promotes tumor evolution in response to genotoxic stress. They also present potential opportunities for therapy that exploit the greater reliance of such cancers on alternative routes of repair.

EXPERIMENTAL PROCEDURES

Cells, DNA plasmids, siRNA, and antibodies and general procedures involving these are described in the [Supplemental Experimental Procedures](#).

GST Affinity Capture and Mass Spectrometry

GST fusion proteins were expressed in *E. coli* and produced as described (Hassler et al., 2007). Purified GST tagged proteins were bound to Glutathione Sepharose 4 Fast Flow resin and used as an affinity matrix for interacting protein capture from nuclear cell extract. Affinity-captured proteins were either assessed using tryptic proteolysis followed by MS analysis (QSTAR Elite, Applied Biosystems) or immunoblotting. Raw MS data were analyzed using Mascot version 2.1 (Matrix Science) followed by Scaffold 3 (Proteome Software).

Co-immunoprecipitation

Nuclear extracts were prepared from purified cell nuclei using micrococcal nuclease to release chromatin-bound protein complexes. Cell nuclei were made as for GST affinity capture. RB1 was immunoprecipitated using rabbit serum against a human RB1 C-terminal fragment (aa 763–928) (Zarkowska and Mittnacht, 1997) crosslinked to Protein A/G Plus Agarose (Thermo Fisher Scientific).

Proximity Ligation Analysis

PLA was performed using Duolink technology (Cambridge Biosciences) in accordance with the manufacturer's recommendations.

γ H2AX Staining and Quantitation

Cells were cultured in black-walled 96-well plates (PerkinElmer) and fixed and processed as described in Richardson et al. (2012). Cells were probed with anti- γ H2AX for 3 hr at room temperature followed by Alexa Fluor 488 fluorescent secondary antibody (Invitrogen) containing 2 μ M Hoechst 33342 (Sigma). Plates were imaged using an automated high-content platform (GE Healthcare). The average intensity (iSig) of the γ H2AX signal was recorded for all individual cells present in six eye fields in each of five wells. The integrated intensity for Hoechst 33342 was extracted using CellProfiler Image analysis freeware.

NHEJ Reporter Assay

NHEJ reporter assays were performed as described (Bennardo et al., 2008). For parallel cell-cycle analysis NHEJ reporter/DsRed-transfected cells were subjected to fluorescence-activated cell sorting for DsRed-positive cells. DsRed-positive cells were subjected to propidium iodide (PI) staining of DNA followed by analysis using flow cytometry. Alternatively, transfected cells were subjected to life-cell staining of DNA using Hoechst 33342 dye. Prior to analysis cells were incubated for 45 min in media containing 10 μ g/ml Hoechst 33342 followed by dual color flow cytometry analysis with data collection gated for DsRed-positive cells. Data for 5,000–10,000 individual cells were collected in each case.

Cell-based assays assessing the effect of RB1 on E2F regulation and cell proliferation are described in the [Supplemental Experimental Procedures](#).

Chromosomal Radiation Sensitivity Analysis

HCT116 cells were transfected with siRNA 48 hr prior to irradiation. Colcemid (Sigma-Aldrich Karyomax) was added at 20 ng/ml 6 hr (HCT116) or 24 hr (MEFs) post IR. Cells were harvested for analysis 16 hr (HCT116) or 28 hr (MEFs) post IR using trypsin. Giemsa-stained metaphase spreads were prepared and analyzed as previously described (Nuta et al., 2014).

Comet Analysis

Cells irradiated on ice were either harvested immediately (0 hr) or following further incubation at 37°C. Cells were embedded in low melting agarose on glass slides followed by lysis in 100 mM EDTA, 2.5 M NaCl, 10 mM Tris-HCl (pH 10.5), 1% Triton X-100 followed by electrophoresis in 50 mM NaOH, 1 mM disodium EDTA (pH 12.5). Slides were stained with propidium iodide, visualized at 20 \times magnification, and analyzed using Comet Analysis software 6.0 (Andor Technology).

Additional details for all experimental procedures are provided in the [Supplemental Experimental Procedures](#).

SUPPLEMENTAL INFORMATION

Supplemental Information includes Supplemental Experimental Procedures, six figures, and four tables and can be found with this article online at <http://dx.doi.org/10.1016/j.celrep.2015.02.059>.

AUTHOR CONTRIBUTIONS

S.M. and P.H.H. planned and supervised the project. R.C., P.H.H., and S.M. wrote the manuscript. R.C., J.A.H, K.R., P.H.H., and S.M. designed experiments. V.J.S. and J.A.H. supervised Comet analysis, K.R. supervised analysis of chromosomal radiation sensitivity performed by J.M. R.C. performed the majority of experiments. G.Z. performed Comet and GST-fusion protein interaction analyses and supported chromosomal radiation sensitivity analysis. M.T.L. contributed to RB1 mutant analysis. S.R. performed cell synchronization experiments. R.C., G.Z., K.R., P.H.H., and S.M. analyzed data.

ACKNOWLEDGMENTS

The authors thank Professor J. M. Stark for providing the NHEJ reporter plasmids, Professor H. teRiele for TKO MEFs, and Drs. S.R. Stockwell and D. Watterskog for support with high-content image analysis. The work was supported through Cancer Research UK (C107/10433 and CRUK/A15043 to S.M. and

C2259/A16569 to J.H.), Worldwide Cancer Research (12-1280 to S.M.) and the Wellcome Trust (WT089028 to P.H.H.). R.C. was supported by an ICR fellowship. J.M. and K.R. were supported by the National Institute for Health Research. The funders had no role in study design, data collection and analysis, decision to publish, or preparation of the manuscript. The views expressed in this publication are those of the authors and not necessarily those of Cancer Research UK, Worldwide Cancer Research, the Wellcome Trust, the NHS, the National Institute for Health Research or the Department of Health.

Received: June 21, 2014

Revised: January 2, 2015

Accepted: February 24, 2015

Published: March 26, 2015

REFERENCES

- Aparicio, T., Baer, R., and Gautier, J. (2014). DNA double-strand break repair pathway choice and cancer. *DNA Repair (Amst.)* 19, 169–175.
- Aydin, O.Z., Vermeulen, W., and Lans, H. (2014). ISWI chromatin remodeling complexes in the DNA damage response. *Cell Cycle* 13, 3016–3025.
- Bennardo, N., Cheng, A., Huang, N., and Stark, J.M. (2008). Alternative-NHEJ is a mechanistically distinct pathway of mammalian chromosome break repair. *PLoS Genet.* 4, e1000110.
- Blanquet, V., Turleau, C., Gross-Morand, M.S., Sénamaud-Beaufort, C., Doz, F., and Besmond, C. (1995). Spectrum of germline mutations in the RB1 gene: a study of 232 patients with hereditary and non hereditary retinoblastoma. *Hum. Mol. Genet.* 4, 383–388.
- Branzei, D., and Foiani, M. (2008). Regulation of DNA repair throughout the cell cycle. *Nat. Rev. Mol. Cell Biol.* 9, 297–308.
- Burma, S., Chen, B.P., and Chen, D.J. (2006). Role of non-homologous end joining (NHEJ) in maintaining genomic integrity. *DNA Repair (Amst.)* 5, 1042–1048.
- Carr, S.M., Munro, S., Zalmas, L.P., Fedorov, O., Johansson, C., Krojer, T., Sargum, C.A., Bedford, M.T., Oppermann, U., and La Thangue, N.B. (2014). Lysine methylation-dependent binding of 53BP1 to the pRB tumor suppressor. *Proc. Natl. Acad. Sci. USA* 111, 11341–11346.
- Chapman, J.R., Taylor, M.R., and Boulton, S.J. (2012). Playing the end game: DNA double-strand break repair pathway choice. *Mol. Cell* 47, 497–510.
- Chew, Y.P., Ellis, M., Wilkie, S., and Mitnacht, S. (1998). pRB phosphorylation mutants reveal role of pRB in regulating S phase completion by a mechanism independent of E2F. *Oncogene* 17, 2177–2186.
- Chiruvella, K.K., Liang, Z., and Wilson, T.E. (2013). Repair of double-strand breaks by end joining. *Cold Spring Harb. Perspect. Biol.* 5, a012757.
- Dannenberg, J.H., van Rossum, A., Schuijff, L., and te Riele, H. (2000). Ablation of the retinoblastoma gene family deregulates G(1) control causing immortalization and increased cell turnover under growth-restricting conditions. *Genes Dev.* 14, 3051–3064.
- Daria, D., Filippi, M.D., Knudsen, E.S., Faccio, R., Li, Z., Kalfa, T., and Geiger, H. (2008). The retinoblastoma tumor suppressor is a critical intrinsic regulator for hematopoietic stem and progenitor cells under stress. *Blood* 111, 1894–1902.
- Dennis, G., Jr., Sherman, B.T., Hosack, D.A., Yang, J., Gao, W., Lane, H.C., and Lempicki, R.A. (2003). DAVID: Database for Annotation, Visualization, and Integrated Discovery. *Genome Biol.* 4, 3.
- Dimaras, H., Khetan, V., Halliday, W., Orlic, M., Prigoda, N.L., Piovesan, B., Marrano, P., Corson, T.W., Eagle, R.C., Jr., Squire, J.A., and Gallie, B.L. (2008). Loss of RB1 induces non-proliferative retinoma: increasing genomic instability correlates with progression to retinoblastoma. *Hum. Mol. Genet.* 17, 1363–1372.
- Doksani, Y., and de Lange, T. (2014). The role of double-strand break repair pathways at functional and dysfunctional telomeres. *Cold Spring Harb. Perspect. Biol.* 6, a016576.
- Fry, D.W., Harvey, P.J., Keller, P.R., Elliott, W.L., Meade, M., Trachet, E., Albassam, M., Zheng, X., Leopold, W.R., Pryer, N.K., and Toogood, P.L. (2004). Specific inhibition of cyclin-dependent kinase 4/6 by PD 0332991 and associated antitumor activity in human tumor xenografts. *Mol. Cancer Ther.* 3, 1427–1438.
- Gonzalez-Vasconcellos, I., Anastasov, N., Sanli-Bonazzi, B., Klymenko, O., Atkinson, M.J., and Rosemann, M. (2013). Rb1 haploinsufficiency promotes telomere attrition and radiation-induced genomic instability. *Cancer Res.* 73, 4247–4255.
- Goodrich, D.W. (2003). How the other half lives, the amino-terminal domain of the retinoblastoma tumor suppressor protein. *J. Cell. Physiol.* 197, 169–180.
- Hassler, M., Singh, S., Yue, W.W., Luczynski, M., Lakbir, R., Sanchez-Sanchez, F., Bader, T., Pearl, L.H., and Mitnacht, S. (2007). Crystal structure of the retinoblastoma protein N domain provides insight into tumor suppression, ligand interaction, and holoprotein architecture. *Mol. Cell* 28, 371–385.
- Hellwinkel, O.J., Müller, J., Pollmann, A., and Kabisch, H. (2005). Osteosarcoma cell lines display variable individual reactions on wildtype p53 and Rb tumour-suppressor transgenes. *J. Gene Med.* 7, 407–419.
- Henley, S.A., and Dick, F.A. (2012). The retinoblastoma family of proteins and their regulatory functions in the mammalian cell division cycle. *Cell Div.* 7, 10.
- Hensey, C.E., Hong, F., Durfee, T., Qian, Y.W., Lee, E.Y., and Lee, W.H. (1994). Identification of discrete structural domains in the retinoblastoma protein. Amino-terminal domain is required for its oligomerization. *J. Biol. Chem.* 269, 1380–1387.
- Heyer, W.D., Ehmsen, K.T., and Liu, J. (2010). Regulation of homologous recombination in eukaryotes. *Annu. Rev. Genet.* 44, 113–139.
- Hilgendorf, K.I., Leshchiner, E.S., Nedelcu, S., Maynard, M.A., Calo, E., Ianari, A., Walensky, L.D., and Lees, J.A. (2013). The retinoblastoma protein induces apoptosis directly at the mitochondria. *Genes Dev.* 27, 1003–1015.
- Hinds, P.W., Mitnacht, S., Dulic, V., Arnold, A., Reed, S.I., and Weinberg, R.A. (1992). Regulation of retinoblastoma protein functions by ectopic expression of human cyclins. *Cell* 70, 993–1006.
- Iliakis, G., Wang, H., Perrault, A.R., Boecker, W., Rosidi, B., Windhofer, F., Wu, W., Guan, J., Terzoudi, G., and Pantelias, G. (2004). Mechanisms of DNA double strand break repair and chromosome aberration formation. *Cytogenet. Genome Res.* 104, 14–20.
- Jacks, T., Fazeli, A., Schmitt, E.M., Bronson, R.T., Goodell, M.A., and Weinberg, R.A. (1992). Effects of an Rb mutation in the mouse. *Nature* 359, 295–300.
- Kakarougkas, A., and Jeggo, P.A. (2014). DNA DSB repair pathway choice: an orchestrated handover mechanism. *Br. J. Radiol.* 87, 20130685.
- Kinashi, Y., Takahashi, S., Kashino, G., Okayasu, R., Masunaga, S., Suzuki, M., and Ono, K. (2011). DNA double-strand break induction in Ku80-deficient CHO cells following boron neutron capture reaction. *Radiat. Oncol.* 6, 106.
- Kleinerman, R.A., Yu, C.L., Little, M.P., Li, Y., Abramson, D., Seddon, J., and Tucker, M.A. (2012). Variation of second cancer risk by family history of retinoblastoma among long-term survivors. *J. Clin. Oncol.* 30, 950–957.
- Kuo, L.J., and Yang, L.X. (2008). Gamma-H2AX - a novel biomarker for DNA double-strand breaks. *In Vivo* 22, 305–309.
- Lee, E.Y., Chang, C.Y., Hu, N., Wang, Y.C., Lai, C.C., Herrup, K., Lee, W.H., and Bradley, A. (1992). Mice deficient for Rb are nonviable and show defects in neurogenesis and haematopoiesis. *Nature* 359, 288–294.
- Lee, J.O., Russo, A.A., and Pavletich, N.P. (1998). Structure of the retinoblastoma tumour-suppressor pocket domain bound to a peptide from HPV E7. *Nature* 391, 859–865.
- Lee, C., Chang, J.H., Lee, H.S., and Cho, Y. (2002). Structural basis for the recognition of the E2F transactivation domain by the retinoblastoma tumor suppressor. *Genes Dev.* 16, 3199–3212.
- Lieber, M.R. (2010). The mechanism of double-strand DNA break repair by the nonhomologous DNA end joining pathway. *Annu. Rev. Biochem.* 79, 181–211.
- Lieber, M.R., Ma, Y., Pannicke, U., and Schwarz, K. (2003). Mechanism and regulation of human non-homologous DNA end joining. *Nat. Rev. Mol. Cell Biol.* 4, 712–720.
- Lohmann, D. (2010). Retinoblastoma. *Adv. Exp. Med. Biol.* 685, 220–227.

- Lohmann, D.R., Gerick, M., Brandt, B., Oelschläger, U., Lorenz, B., Passarge, E., and Horsthemke, B. (1997). Constitutional RB1-gene mutations in patients with isolated unilateral retinoblastoma. *Am. J. Hum. Genet.* *61*, 282–294.
- Malu, S., Malshetty, V., Francis, D., and Cortes, P. (2012). Role of non-homologous end joining in V(D)J recombination. *Immunol. Res.* *54*, 233–246.
- Manning, A.L., and Dyson, N.J. (2012). RB: mitotic implications of a tumour suppressor. *Nat. Rev. Cancer* *12*, 220–226.
- Meadows, A.T., Friedman, D.L., Neglia, J.P., Mertens, A.C., Donaldson, S.S., Stovall, M., Hammond, S., Yasui, Y., and Inskip, P.D. (2009). Second neoplasms in survivors of childhood cancer: findings from the Childhood Cancer Survivor Study cohort. *J. Clin. Oncol.* *27*, 2356–2362.
- Mellacheruvu, D., Wright, Z., Couzens, A.L., Lambert, J.P., St-Denis, N.A., Li, T., Miteva, Y.V., Hauri, S., Sardiou, M.E., Low, T.Y., et al. (2013). The CRAPome: a contaminant repository for affinity purification-mass spectrometry data. *Nat. Methods* *10*, 730–736.
- Miller, K.M., Tjeertes, J.V., Coates, J., Legube, G., Polo, S.E., Britton, S., and Jackson, S.P. (2010). Human HDAC1 and HDAC2 function in the DNA-damage response to promote DNA nonhomologous end joining. *Nat. Struct. Mol. Biol.* *17*, 1144–1151.
- Negrini, S., Gorgoulis, V.G., and Halazonetis, T.D. (2010). Genomic instability—an evolving hallmark of cancer. *Nat. Rev. Mol. Cell Biol.* *11*, 220–228.
- Nuta, O., Moquet, J., Bouffler, S., Lloyd, D., Sepai, O., and Rothkamm, K. (2014). Impact of long-term exposure to sodium arsenite on cytogenetic radiation damage. *Mutagenesis* *29*, 123–129.
- Panier, S., and Boulton, S.J. (2014). Double-strand break repair: 53BP1 comes into focus. *Nat. Rev. Mol. Cell Biol.* *15*, 7–18.
- Papamichos-Chronakis, M., and Peterson, C.L. (2013). Chromatin and the genome integrity network. *Nat. Rev. Genet.* *14*, 62–75.
- Richardson, E., Stockwell, S.R., Li, H., Aherne, W., Cuomo, M.E., and Mittnacht, S. (2012). Mechanism-based screen establishes signalling framework for DNA damage-associated G1 checkpoint response. *PLoS ONE* *7*, e31627.
- Rothkamm, K., Krüger, I., Thompson, L.H., and Löbrich, M. (2003). Pathways of DNA double-strand break repair during the mammalian cell cycle. *Mol. Cell Biol.* *23*, 5706–5715.
- Sampieri, K., Mencarelli, M.A., Epistolato, M.C., Toti, P., Lazzi, S., Bruttini, M., De Francesco, S., Longo, I., Meloni, I., Mari, F., et al. (2008). Genomic differences between retinoma and retinoblastoma. *Acta Oncol.* *47*, 1483–1492.
- Schaal, C., Pillai, S., and Chellappan, S.P. (2014). The Rb-E2F transcriptional regulatory pathway in tumor angiogenesis and metastasis. *Adv. Cancer Res.* *121*, 147–182.
- Schmitt, M.W., Prindle, M.J., and Loeb, L.A. (2012). Implications of genetic heterogeneity in cancer. *Ann. N Y Acad. Sci.* *1267*, 110–116.
- Shuin, T., Torigoe, S., Kubota, Y., Kishida, T., Hosaka, M., Horikoshi, T., Yao, M., Kondo, K., Sakai, N., Danenberg, K., et al. (1995). Retinoblastoma gene mutation in primary human renal cell carcinoma. *Oncol. Res.* *7*, 63–66.
- Talluri, S., and Dick, F.A. (2012). Regulation of transcription and chromatin structure by pRB: here, there and everywhere. *Cell Cycle* *11*, 3189–3198.
- Thériault, B.L., Dimaras, H., Gallie, B.L., and Corson, T.W. (2014). The genomic landscape of retinoblastoma: a review. *Clin. Experiment. Ophthalmol.* *42*, 33–52.
- Tuzon, C.T., Spektor, T., Kong, X., Congdon, L.M., Wu, S., Schotta, G., Yokomori, K., and Rice, J.C. (2014). Concerted activities of distinct H4K20 methyltransferases at DNA double-strand breaks regulate 53BP1 nucleation and NHEJ-directed repair. *Cell Rep.* *8*, 430–438.
- Vandersickel, V., Depuydt, J., Van Bockstaele, B., Perletti, G., Philippe, J., Thierens, H., and Vral, A. (2010). Early increase of radiation-induced γ H2AX foci in a human Ku70/80 knockdown cell line characterized by an enhanced radiosensitivity. *J. Radiat. Res. (Tokyo)* *51*, 633–641.
- Viatur, P., Somerville, T.C., Venkatasubrahmanyam, S., Kogan, S., McLaughlin, M.E., Weissman, I.L., Butte, A.J., Passequé, E., and Sage, J. (2008). Hematopoietic stem cell quiescence is maintained by compound contributions of the retinoblastoma gene family. *Cell Stem Cell* *3*, 416–428.
- Walkley, C.R., and Orkin, S.H. (2006). Rb is dispensable for self-renewal and multilineage differentiation of adult hematopoietic stem cells. *Proc. Natl. Acad. Sci. USA* *103*, 9057–9062.
- Weibrecht, I., Leuchowius, K.J., Clausson, C.M., Conze, T., Jarvius, M., Howell, W.M., Kamali-Moghaddam, M., and Söderberg, O. (2010). Proximity ligation assays: a recent addition to the proteomics toolbox. *Expert Rev. Proteomics* *7*, 401–409.
- Wong, J.R., Morton, L.M., Tucker, M.A., Abramson, D.H., Seddon, J.M., Sampson, J.N., and Kleinerman, R.A. (2014). Risk of subsequent malignant neoplasms in long-term hereditary retinoblastoma survivors after chemotherapy and radiotherapy. *J. Clin. Oncol.* *32*, 3284–3290.
- Woodbine, L., Gennery, A.R., and Jeggo, P.A. (2014). The clinical impact of deficiency in DNA non-homologous end joining. *DNA Repair (Amst.)* *16*, 84–96.
- Xiao, B., Spencer, J., Clements, A., Ali-Khan, N., Mittnacht, S., Broceño, C., Burghammer, M., Perrakis, A., Marmorstein, R., and Gamblin, S.J. (2003). Crystal structure of the retinoblastoma tumor suppressor protein bound to E2F and the molecular basis of its regulation. *Proc. Natl. Acad. Sci. USA* *100*, 2363–2368.
- Yang, Y., Tian, S., Brown, B., Chen, P., Hu, H., Xia, L., Zhang, J., Cai, X., Chen, Z., Pan, X., et al. (2013). The Rb1 gene inhibits the viability of retinoblastoma cells by regulating homologous recombination. *Int. J. Mol. Med.* *32*, 137–143.
- Zarkowska, T., and Mittnacht, S. (1997). Differential phosphorylation of the retinoblastoma protein by G1/S cyclin-dependent kinases. *J. Biol. Chem.* *272*, 12738–12746.
- Zhao, Y., Thomas, H.D., Batey, M.A., Cowell, I.G., Richardson, C.J., Griffin, R.J., Calvert, A.H., Newell, D.R., Smith, G.C., and Curtin, N.J. (2006). Preclinical evaluation of a potent novel DNA-dependent protein kinase inhibitor NU7441. *Cancer Res.* *66*, 5354–5362.

Cell Reports

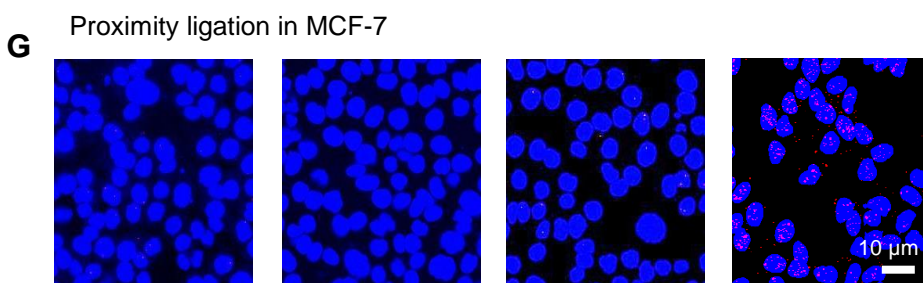
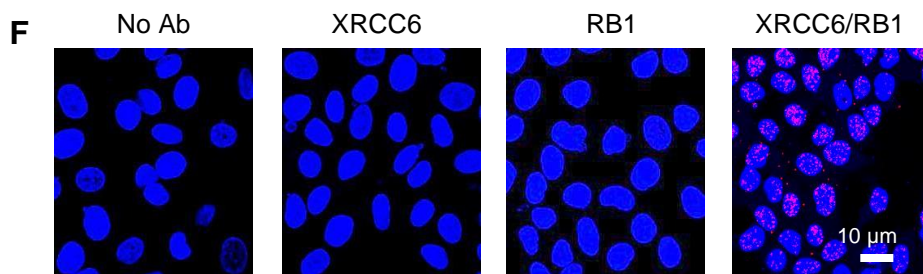
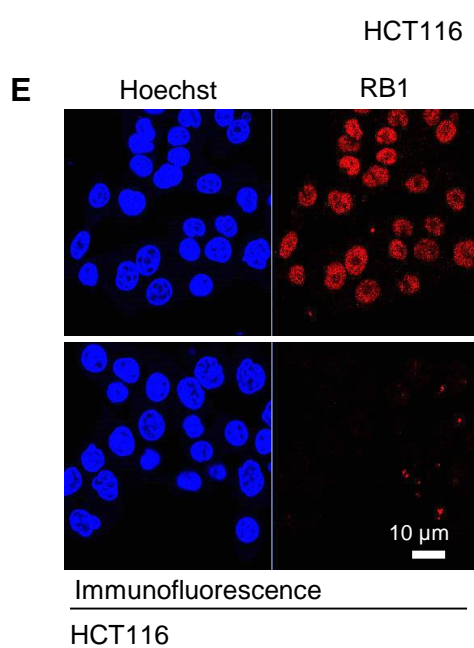
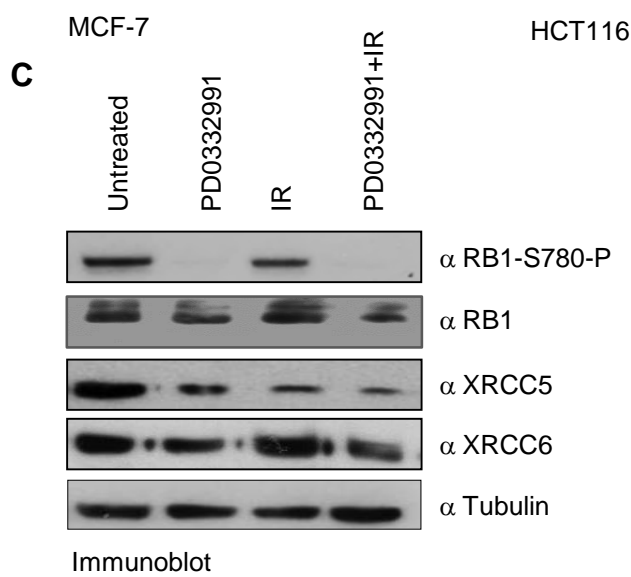
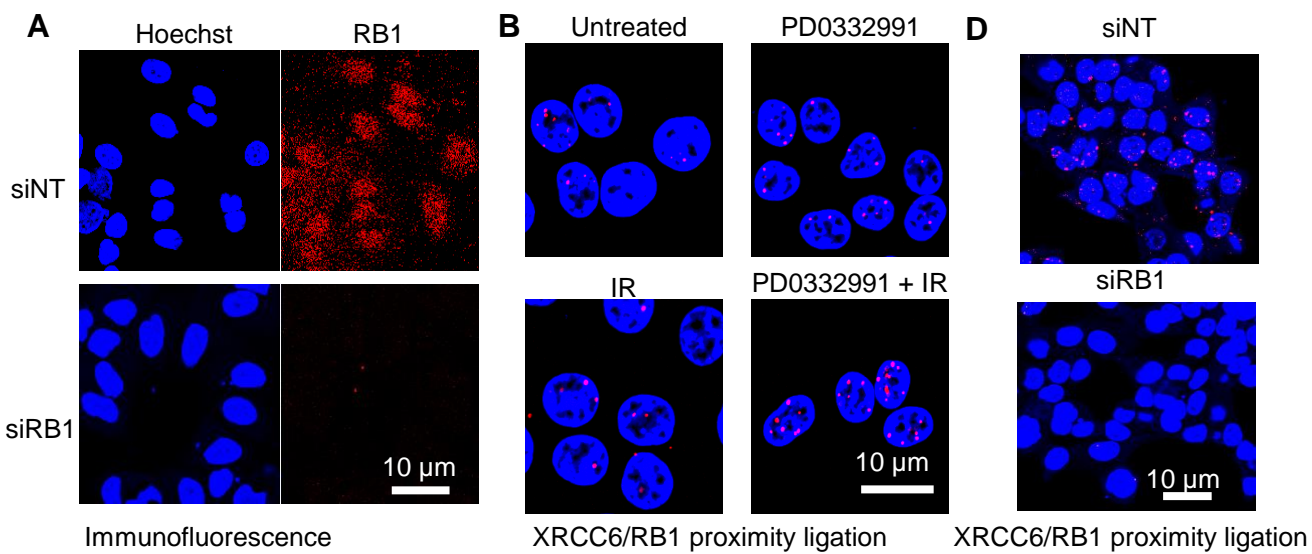
Supplemental Information

Direct Involvement of Retinoblastoma

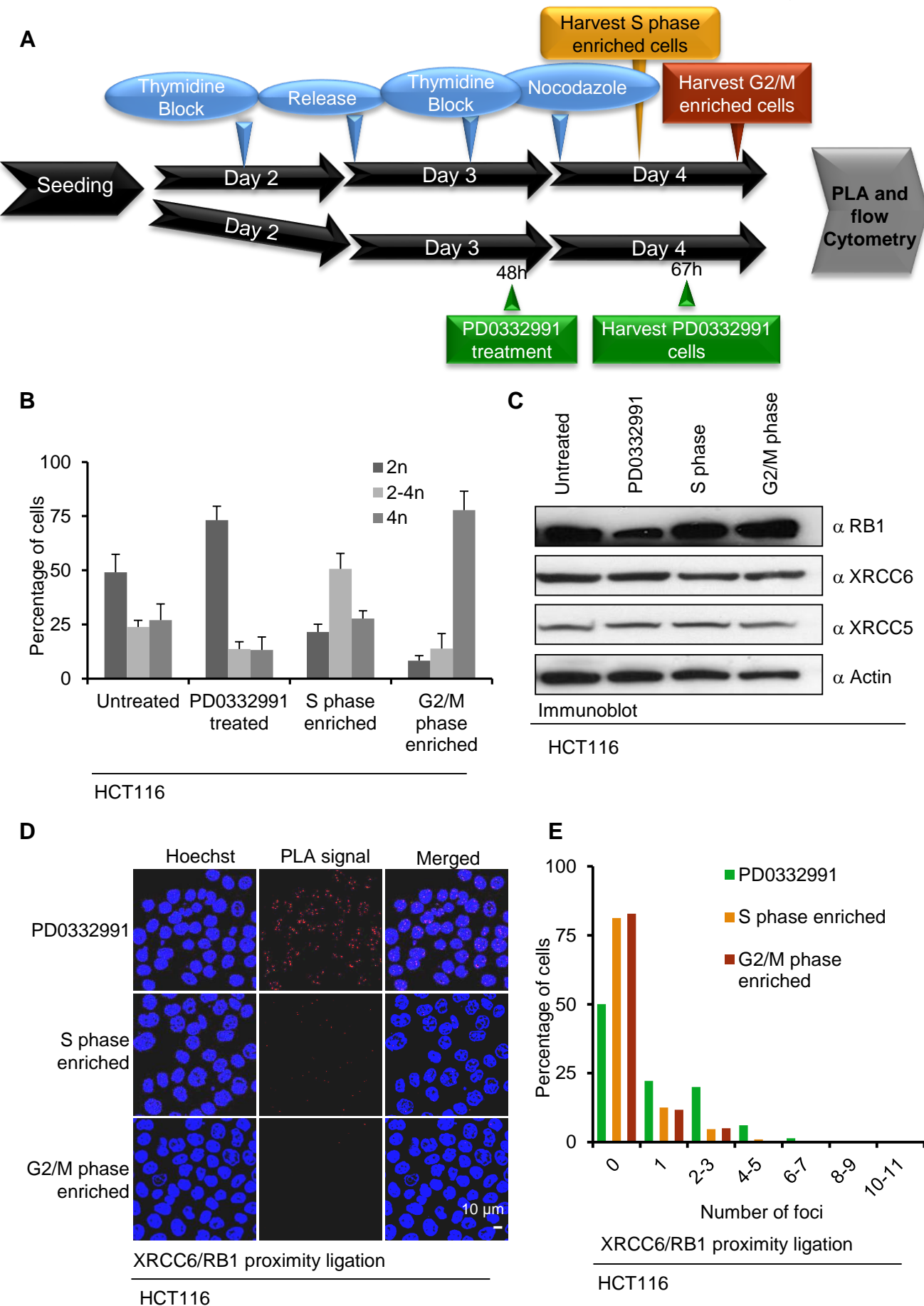
Family Proteins in DNA Repair

by Non-homologous End Joining

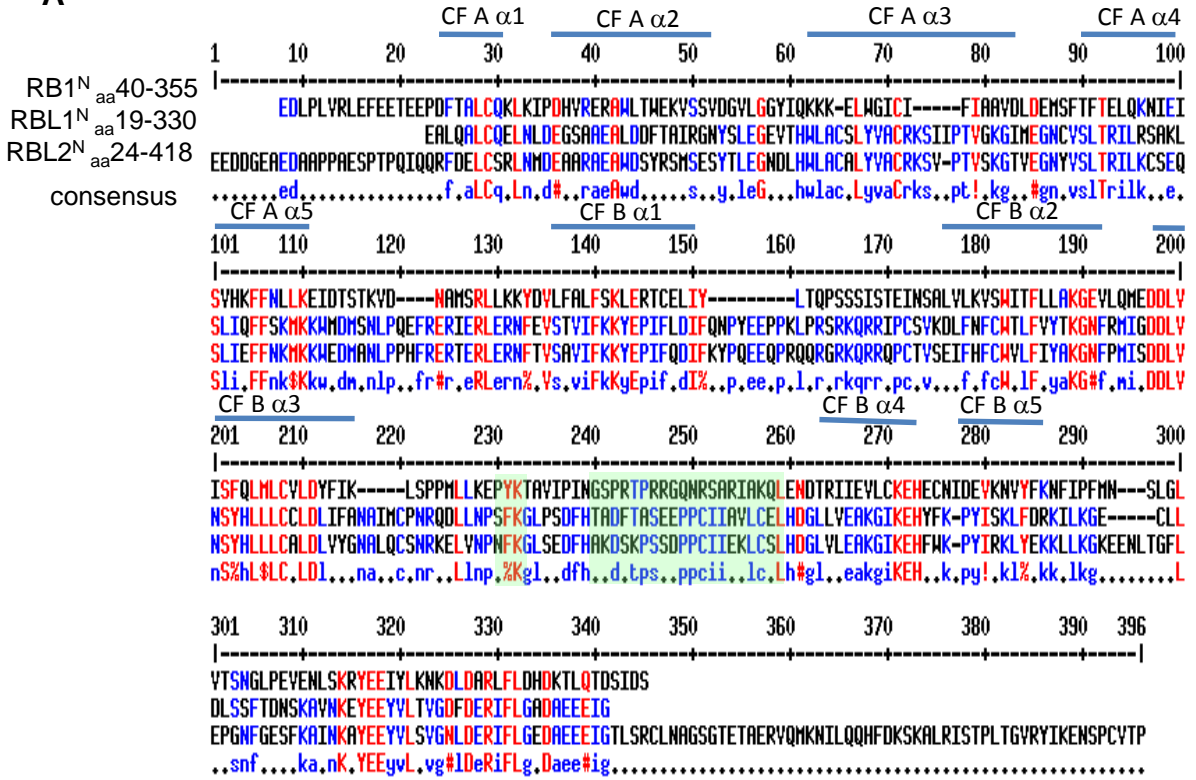
Rebecca Cook, Georgia Zoumpoulidou, Maciej T. Luczynski, Simone Rieger, Jayne Moquet, Victoria J. Spanswick, John A. Hartley, Kai Rothkamm, Paul H. Huang, and Sibylle Mittnacht



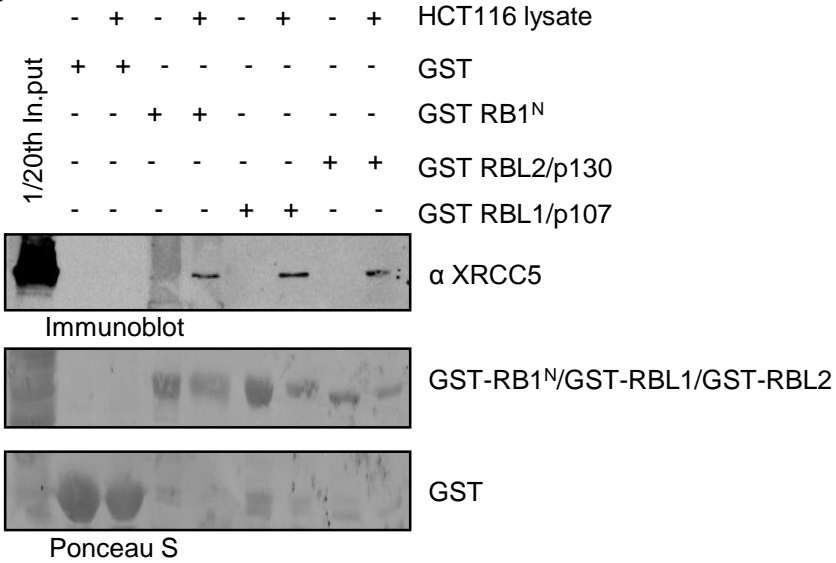
Proximity ligation in HCT116

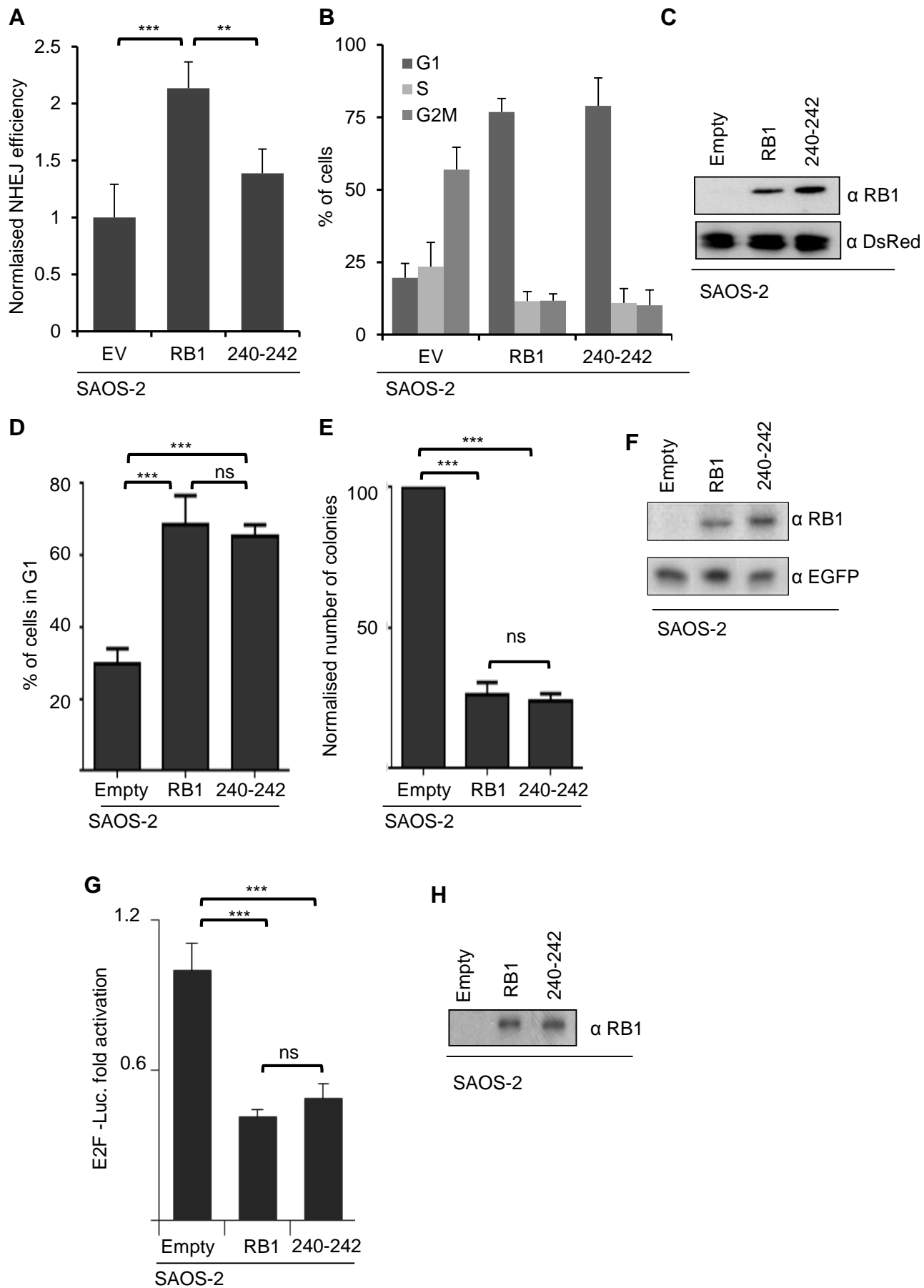


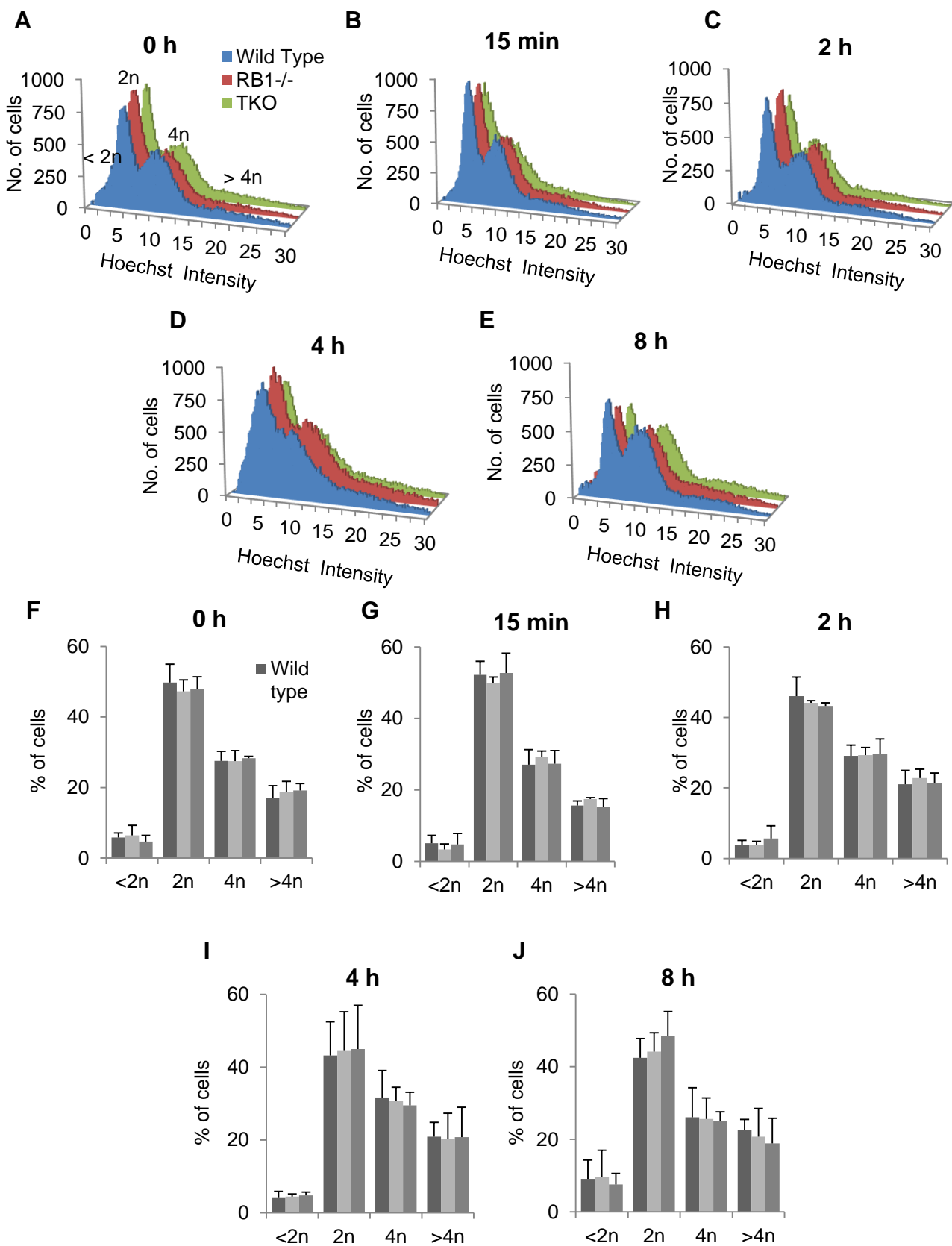
A

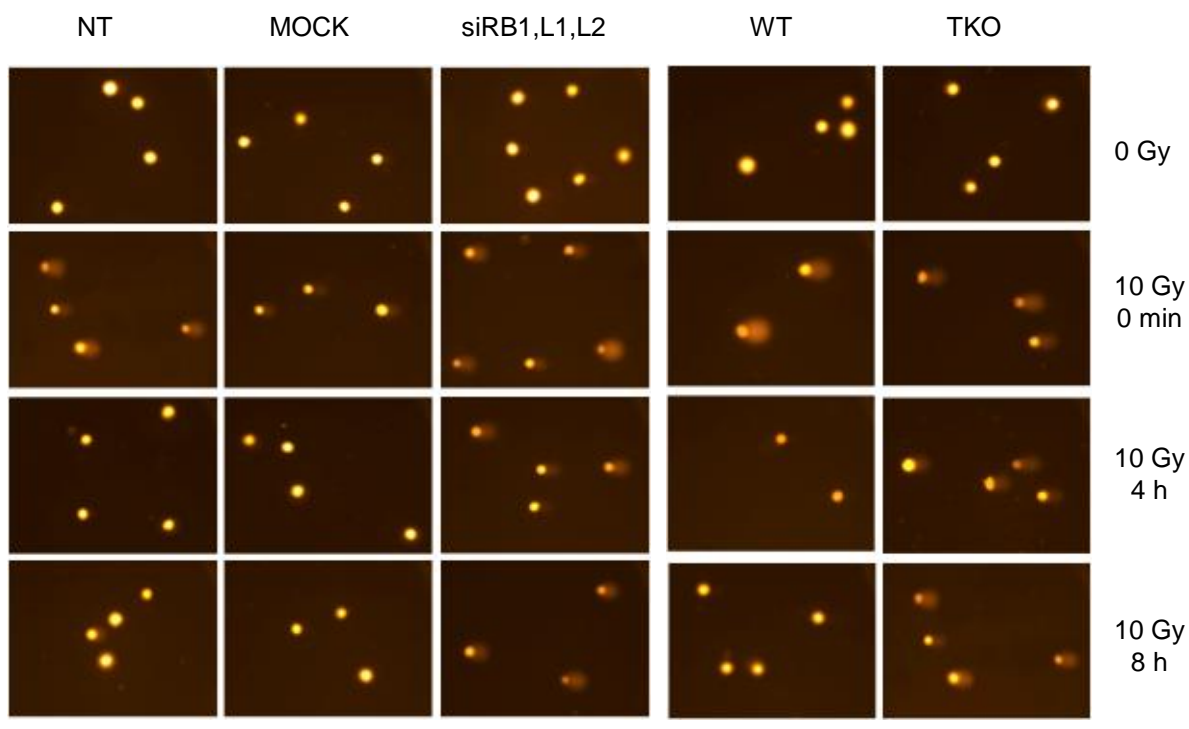


B







A

HCT116

MEFs

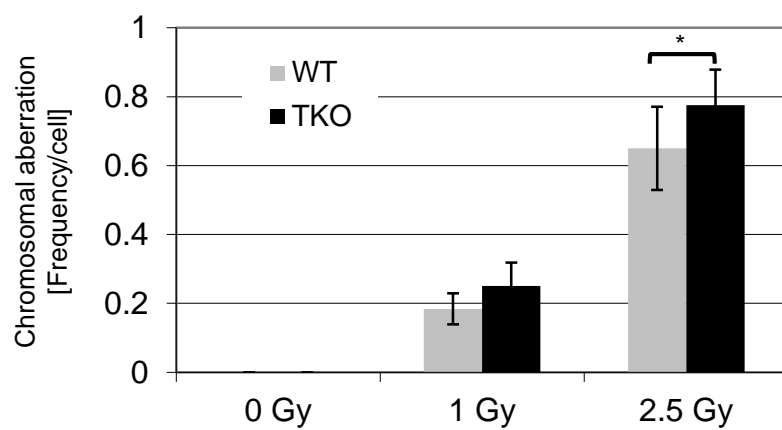
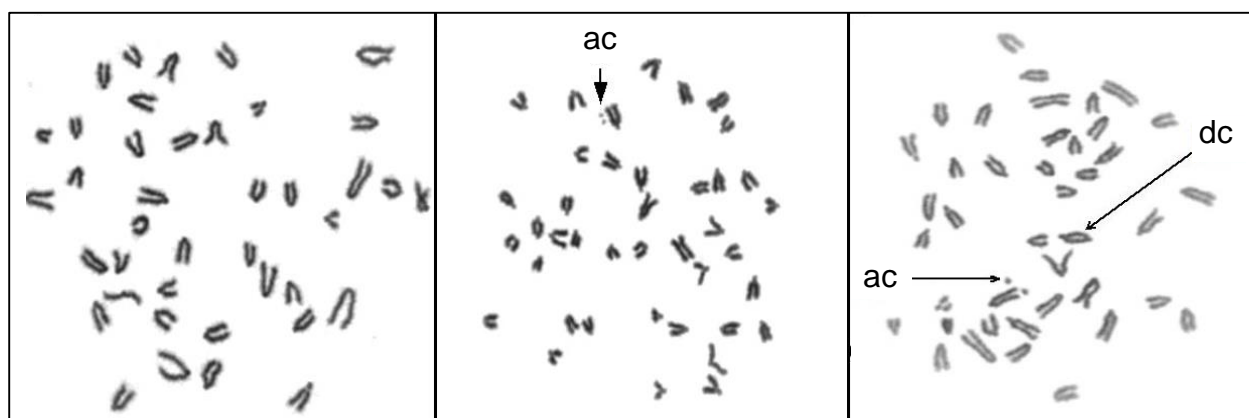
B**C**

Figure S1: Interaction between XRCC6 and RB1 in MCF-7 and HCT116 cells, Related to Figure 2

(A) RB1 immunofluorescence detection. MCF-7 cells transfected and treated in parallel and as for Figure 2D. The expression of RB1 was determined by immunofluorescence (red). Nuclei were visualised with Hoechst 33258.

(B) Proximity ligation probing for XRCC6/RB1 complex in HCT116 cells. Cells were subjected to treatment and processed as for Figure 2A. Signals pertinent to XRCC6/RB1 interactions are in red. Nuclei were visualised with Hoechst 33258. Scale bar represents 10 μm .

(C) Immunoblotting analysis of P-Ser780 RB1, serving as a biomarker for CDK4/6 activity. XRCC5 and XRCC6 total protein levels were also assessed. RB1 protein levels and tubulin levels are shown as loading controls. Cells were treated in parallel with, and as described for, samples analysed for Figure S1B.

(D) Proximity ligation probing for XRCC6/RB1 complexes in HCT116 cells treated with non-targeting (siNT) or RB1 targeting siRNA. Cells were treated and processed as for Figure 2D.

(E) RB1 Immunofluorescence detection. The expression of RB1 was determined by immunofluorescence (red). HCT116 cells transfected as in (D). Nuclei were visualised with Hoechst 33258. Scale bar represent 10 μm .

(F and G) Proximity ligation control reactions carried out in MCF-7 cells (F) and HCT116 cells (G). Either secondary probes alone (no Ab) were used, or secondary probes in combination with primary antibodies for XRCC6 or RB1 individually or in combination. Nuclei were visualised with Hoechst 33258. Samples were run in parallel with those shown in Figure 2A (MCF-7 cells) and Figure S1G (HCT116 cells). Scale bars show 10 μm .

Figure S2: Cell synchronisation and PLA staining, Related to Figure 2

(A) Workflow diagram for generation of cell cycle synchronised cell populations. MCF-7 and HCT116 were enriched for cells in G1, mid-S or G2/M phase of the cell cycle. S phase and G2/M enriched cell populations were generated using a double thymidine block (2 μ M) followed by release into medium containing nocodazole (100 nM). Cells were harvested either 2 h (HCT116 mid-S phase enriched)/ 3 h (MCF-7 mid-S phase enriched) or 8 h later (HCT116 G2/M phase enriched)/ 10 h (MCF-7 G2/M phase enriched). Alternatively, cells seeded in parallel were exposed to 400 nM PD0332991 for 17 h (HCT116) or 19 h (MCF7).

(B) Cell cycle profiles of HCT116 subjected to procedures in (A), as determined by propidium iodide staining and flow cytometry. Error bars represent \pm S.D for n = 3 biological replicates.

(C) Immunoblotting analysis depicting levels of RB1, XRCC5 and XRCC6 protein. Actin levels are shown as loading controls.

(D) Detection of RB1/XRCC6 complex in cell cycle phase enriched HCT116 cells. Complexes were detected using proximity ligation. Nuclei were visualised with Hoechst 33258.

(E) Automated quantification of foci number. Cumulative data for n=3 biological replicates are shown, representing quantification for a minimum of 100 independent cells. Quantification was performed as for Figure 2B, F.

Figure S3: Interaction of NHEJ component XRCC6 with RB family proteins, Related to Figure 3

(A) RB family protein sequence alignment. Sequences represent GST fusion proteins used in (B). The Alignments were generated using MultAlin V5, with hierarchical clustering for maximal amino acid similarity. Consensus levels: red = 100 % blue = 66 %. Consensus symbols: ! Either Ile or Val ; \$ either Leu or Met; % either Phe or Tyr; # any of Asn, Asp, Gln or Gl. The position of sequence alterations (240-242 deletion and PolyG) associated with loss of interaction between RB1 to XRCC6 indicated by green coloured overly. The position of the cyclin fold helixes α 1- α 5 generating cyclin fold (CF) scaffolds A and CF scaffold B in RB1 N are indicated. CF A; cyclin fold A, CF B; cyclin fold B.

(B) Affinity enrichment analysis. Experiments were done using conditions as in Figure 1B-G. Purified recombinant RB family proteins N domain fragments (RB1 (aa 40-355), RBL1 (aa 19-330), RBL2 (aa 24-418) were expressed fused to GST and purified. Fusion proteins bound to Glutathione-resin were incubated with chromatin extract from 1×10^6 HCT116 cells as for Figure 1. Bound material was assessed for the presence of the NHEJ component XRCC5. GST alone was used as a negative control.

Figure S4: A role for RB1^N in NHEJ, Related to Figure 4

(A) NHEJ proficiency in SAOS-2 cells transfected with empty vector or vector expressing RB1 or RB1^{240-242deletion} variant. Data evaluation was as for Figure 4. Values for cells transfected with empty vector were set to 1.

(B) Cell cycle profiles of reporter transfected SAOS-2 cells, analysed as for Figure 4B. Profiles with a secondary nocodazole block are shown. Data represent transfected cell fractions deduced using DsRed for gating.

(C) Immunodetection of RB1 and RB1²⁴⁰⁻²⁴² in SAOS-2 cells from (A), loading was normalised for co-transfected DsRed expression plasmid.

(D) Proficiency of 240-242 to inhibit cell cycle progression in SAOS-2. Graph depicts stable G1 arrest, assessed by propidium iodide flow cytometry in cells with secondary nocodazole block. SAOS-2 cells transfected with empty vector, RB1 or 240-242 expression vectors.

(E) Proficiency of RB1²⁴⁰⁻²⁴² to inhibit colony formation. SAOS-2 transfected with empty vector, RB1 or 240-242 expression vector in combination with vector for puromycin resistance and scored for outgrowth of puromycin resistant colonies. Co-transfected β -galactosidase was used to normalise data to transfection efficacy.

(F) Immunodetection of RB1 and RB1²⁴⁰⁻²⁴² in SAOS-2 used in (D and E), loading was normalised using co-transfected EGFP expression plasmid.

(G) Proficiency of RB1²⁴⁰⁻²⁴² to regulated E2F activity. E2F reporter activity in SAOS-2 cells. Cells were transfected with RB1 or 240-242 or empty expression vector together with E2F promoter luciferase reporter. Co-transfected β -galactosidase was used to normalise data to transfection efficacy.

(H) Immunodetection of RB1 and RB1²⁴⁰⁻²⁴² in SAOS-2 used in (G). Loading was normalized to β -galactosidase activity. For all experiments the average for n = 3 biological replicates is depicted, error bars \pm S.D * p<0.05 ** p<0.01 ***p<0.001 using a paired Student's t-test.

Figure S5: DNA content profiles of MEFs over irradiation time course, Related to Figure 5

(A-E) Integrated Hoechst 33258 staining intensity histogram for the three MEF backgrounds at various time points post 5 Gy IR. Wild type, RB1^{-/-} or RB1/RBL1/RBL2 null (TKO) mouse embryonic fibroblasts (MEFs) were exposed to 5 Gy IR and stained for γ H2AX and

DNA (using Hoechst 33258). Hoechst 33258 staining intensity (integrated mean) was determined for all cells from 30 independent eye fields and the distributions from one representative experiment are shown (A-E).

(F-J) Percentage of cells with $< 2n$, $2n$, $4n$ and $> 4n$ DNA content determined by gating (dotted line). Error bars represent \pm S.D for $n = 3$ biological replicates.

Figure S6: Effect of RB family loss on DSB repair, Related to Figure 6

(A) Single cell comet analysis. HCT116 with and without siRNA-mediated ablation of RB family proteins (left) and congenic normal MEFs (wt) and MEFs with RB family gene deletion (TKO). Representative raw images are shown. Data relate to Figure 6A.

(B) Chromosomal aberration analysis in MEFs. Data for normal MEFs (wt) and MEFs with RB family gene deletion (TKO) are shown. Bars represent the frequency of cytogenetic aberrations detected per cell, considering both chromosome and chromatid aberrations. For each condition $n = 50$ metaphases were scored. Error bars represent SEM. For raw numerical scores see Table S4.

(C) Examples of Giemsa-stained MEF metaphases used for chromosome aberration analysis shown in B. Aberrations denoted by arrows, dicentrics (dc), excess acentric (ac).

| Name | Uniprot Accession | Scaffold Probability | Mascot Score | Unique Peptides | Sequence Coverage (%) |
|---|-------------------|----------------------|--------------|-----------------|-----------------------|
| DNA-dependent protein kinase catalytic subunit (PRKDC) | P78527 | 99.97 | 2299.7 | 13.33 | 47 |
| Very long-chain specific acyl-CoA dehydrogenase (ACADV) | P49748 | 100 | 2016 | 49 | 27 |
| ATP-dependent DNA helicase 2 subunit 2 (XRCC5) | P13010 | 100 | 1420.3 | 45.4 | 27.33 |
| ATP-dependent DNA helicase 2 subunit 1 (XRCC6) | P12956 | 100 | 1174.7 | 40 | 23.33 |
| Lamin-A/C (LMNA) | P02545 | 100 | 515.3 | 26 | 16 |
| Poly [ADP-ribose] polymerase 1 (PARP1) | P09874 | 100 | 494 | 17.2 | 13.7 |
| 60 kDa heat shock protein (CH60) | P10809 | 100 | 435 | 26 | 11.33 |
| Heterogeneous nuclear ribonucleoprotein M (HNRPM) | P52272 | 100 | 332.7 | 12.57 | 8.33 |
| Histone H1.2 (H12) | P16403 | 99.93 | 275.3 | 19.13 | 5.67 |
| Probable ATP-dependent RNA helicase DDX5 (DDX5) | P17844 | 100 | 246 | 9.5 | 6.37 |
| TAR DNA-binding protein (TADBP) | Q13148 | 99.93 | 156.3 | 8.6 | 3 |
| Histone H1.5 (H15) | P16401 | 100 | 150.7 | 13 | 3.33 |
| DNA ligase 3 (DNLI3) | P49916 | 100 | 107.3 | 4.37 | 3.67 |
| Nucleolar RNA helicase 2 (DDX21) | Q9NR30 | 100 | 100.7 | 5.27 | 2.67 |
| Synaptic vesicle membrane protein VAT-1 homolog (VAT1) | Q99536 | 99.93 | 98.3 | 7.83 | 2.33 |
| Carbamoyl-phosphate synthase (CPSM) | P31327 | 100 | 95 | 2.27 | 3.33 |
| Serine hydroxymethyltransferase (GLYM) | P34897 | 100 | 91.3 | 10.3 | 4 |
| Heterogeneous nuclear ribonucleoprotein A1 (ROA1) | P09651 | 99.7 | 81.7 | 7.13 | 1.67 |
| Tubulin alpha-1A chain (TBA1A) | Q71U36 | 99 | 81 | 7.17 | 2.33 |
| Ribonucleoprotein PTB-binding 1 (RAVR1) | Q8IY67 | 99.9 | 79.7 | 5.7 | 2.33 |
| Bifunctional methylenetetrahydrofolate dehydrogenase (MTDC) | P13995 | 99.8 | 76.3 | 7.5 | 1 |
| Serine/threonine-protein kinase PLK1 (PLK1) | P53350 | 99.5 | 76.3 | 3 | 1.67 |
| Elongation factor Tu (EFTU) | P49411 | 99.85 | 71.3 | 3.6 | 1.3 |
| Mitochondrial ribonuclease P protein 1 (MRRP1) | Q7L0Y3 | 100 | 65.7 | 4.23 | 1.67 |
| Medium-chain specific acyl-CoA dehydrogenase (ACADM) | P11310 | 99.85 | 63.7 | 3.57 | 1.33 |
| Matrin-3 (MATR3) | P43243 | 100 | 58.7 | 2.5 | 1.67 |
| Tubulin beta chain (TBB5) | P07437 | 99.5 | 58.7 | 3.9 | 1.33 |
| T-complex protein 1 subunit gamma (TCPG) | P49368 | 99 | 57.3 | 2.57 | 1.33 |
| ATP-dependent RNA helicase DDX39 (DDX39) | O00148 | 100 | 57 | 3.6 | 1.33 |
| L-lactate dehydrogenase A chain (LDHA) | P00338 | 99 | 56.7 | 3.2 | 1 |
| Signal recognition particle 72 kDa protein (SRP72) | O76094 | 99.4 | 51 | 2.23 | 1 |
| Histone-binding protein RBBP7 (RBBP7) | Q16576 | 99.9 | 50.7 | 2.43 | 1 |
| Nucleophosmin (NPM) | P06748 | 100 | 45.3 | 9.83 | 1.3 |
| Ras GTPase-activating-like protein (IQGA1) | P46940 | 99.8 | 42.3 | 0.87 | 1.33 |

Table S1. Table of RB1^N interactors, Related to Figure 1. Table S1 lists candidate proteins found to interact with RB1^N in two or more repeat pulldown reactions, ranked by their average Mascot score. The average probability as determined by Scaffold 3, the percent average sequence coverage and average number of unique peptides for each candidate protein is shown.

| Condition A | Condition B | P value |
|---------------------|----------------------------------|----------------|
| Untreated | PD0339921 treatment | 0.005 |
| Untreated | 5 Gy IR | <0.0001 |
| Untreated | 5 Gy IR plus PD0339921 treatment | <0.0001 |
| PD0339921 treatment | 5 Gy IR | 0.211464 |
| PD0339921 treatment | 5 Gy IR plus PD0339921 treatment | <0.0001 |
| 5 Gy IR | 5 Gy IR plus PD0339921 treatment | <0.0001 |

Table S2. Statistical test results for PLA detecting the interaction between RB1 and XRCC6 in MCF-7 cells, Related to Figure 2. Table S2 lists p-values from pair-wise comparison of population data depicted in Figure 2B, as determined by the Mann Whitney U test.

| Condition A | Condition B | MCF-7 cells P value | HCT116 cells P value |
|------------------|---------------------|------------------------|-------------------------|
| G1 enriched | S phase enriched | <0.001 | <0.001 |
| G1 enriched | G2/M phase enriched | <0.001 | <0.001 |
| S phase enriched | G2/M phase enriched | 0.0104 | 0.2454 |

Table S3. Statistical test results for PLA detecting the interaction between RB1 and XRCC6 in cell cycle phase enriched MCF7 and HCT116 populations, Related to Figure 2. Table S3 lists p-values from pair-wise comparison of population data depicted in Figure 2F and Figure S2E, as determined by the Mann Whitney U test.

| Cells | Dose (Gy) | Total cells scored | Normal | Chromosome aberrations | | | | Chromatid aberration | | | | | Mitotic Index |
|------------------|-----------|--------------------|--------|------------------------|---------------|------------------|-------------------|----------------------|------------------|--------------------|---------------------|-----------------|---------------|
| | | | | Dicentric | Dentric rings | Excess acentrics | Total chromosomal | Chromatid gaps | Chromatid breaks | Iso chromatid gaps | Chromatid exchanges | Total chromatid | |
| MEFs Wild- type | 0 | 50 | 49 | 0 | 0 | 0 | 0 | 0 | 1 | 0 | 0 | 1 | 3.2 |
| | 1 | 50 | 38 | 4 | 0 | 5 | 9 | 1 | 2 | 0 | 0 | 3 | 0.6 |
| | 2.5 | 50 | 26 | 3 | 0 | 29 | 33 | 3 | 2 | 0 | 0 | 4 | 0.4 |
| MEFs TKO | 0 | 50 | 49 | 0 | 0 | 0 | 0 | 0 | 2 | 0 | 0 | 2 | 4.6 |
| | 1 | 50 | 38 | 2 | 1 | 12 | 14 | 2 | 1 | 0 | 0 | 4 | 4.8 |
| | 2.5 | 50 | 27 | 6 | 0 | 33 | 39 | 1 | 1 | 0 | 1 | 3 | 1.8 |
| HCT116 NT | 0 | 50 | 41 | 0 | 0 | 1 | 1 | 1 | 7 | 0 | 0 | 8 | 28.0 |
| | 1 | 50 | 28 | 6 | 0 | 15 | 21 | 5 | 7 | 0 | 0 | 12 | 22.0 |
| | 2.5 | 50 | 18 | 25 | 0 | 37 | 62 | 3 | 3 | 1 | 0 | 7 | 11.4 |
| HCT116 MOCK | 0 | 50 | 46 | 0 | 0 | 0 | 0 | 1 | 2 | 1 | 0 | 4 | 26.2 |
| | 1 | 50 | 32 | 5 | 0 | 13 | 18 | 3 | 2 | 0 | 0 | 5 | 21.7 |
| | 2.5 | 50 | 14 | 15 | 0 | 25 | 40 | 3 | 7 | 1 | 1 | 12 | 15.1 |
| HCT116 LIG4 | 0 | 50 | 45 | 0 | 0 | 0 | 0 | 1 | 3 | 0 | 0 | 4 | 29.9 |
| | 1 | 50 | 27 | 7 | 0 | 12 | 19 | 5 | 8 | 0 | 0 | 13 | 21.5 |
| | 2.5 | 50 | 11 | 19 | 0 | 43 | 62 | 4 | 10 | 0 | 2 | 16 | 9.1 |
| HCT116 RB1,L1,L2 | 0 | 50 | 45 | 0 | 0 | 1 | 1 | 0 | 4 | 0 | 0 | 4 | 34.1 |
| | 1 | 50 | 29 | 2 | 0 | 14 | 16 | 6 | 16 | 0 | 0 | 22 | 31.6 |
| | 2.5 | 50 | 14 | 18 | 0 | 32 | 50 | 2 | 12 | 0 | 1 | 15 | 16.8 |

Table S4. Chromosomal radiation sensitivity data summary, Related to Figure 6. Table S4 summarises type and frequencies of chromosome and chromatid aberrations in first post-irradiation metaphases, related to supplemental Figure S6 (MEF data) and Figure 6 (HCT116 data).

SUPPLEMENTAL EXPERIMENTAL PROCEDURES

GST fusion protein purification. RosettaTM *E. coli* (Merck) were transformed with relevant GST constructs. Expression was induced with 200 μ M IPTG (Sigma) at A₆₀₀ = 0.6-0.7 at 20 °C for 18 h. Induced *E. coli* bacteria were sedimented by centrifugation and resuspended in extraction buffer (20 mM Tris-Cl pH 7.5, 80 mM NaCl, 5 mM DTT, 1 mM EDTA) with one complete protease inhibitor tablet (Roche). Suspensions were sonicated until the bacteria lysed, and cleared by centrifugation (20,000 g) for 1 h at 4 °C. For large scale preparations supernatants were purified using Q-Sepharose, followed by Glutathione Sepharose4 Fast Flow resin (GE Healthcare). Fusion proteins were bound to the resin in extraction buffer supplemented with 10 mM MgCl₂, 1 mM MnCl₂, 50 U/ml DNase I and 14 U/ml RNase A and eluted with reduced L-Glutathione (Sigma). Eluted preparations were dialysed into 20 mM Tris pH 7.5, 50 mM NaCl, 5 mM DTT and 1 mM EDTA. Protein concentrations were estimated by UV-Spectroscopy.

Mass spectrometry. GST affinity purified material was run into a 12 % Bis-Tris gel (Invitrogen), the protein containing region was excised as a single fraction, the gel slice was washed with 100 mM ammonium bicarbonate treated with 20 mM dithiothreitol (Sigma) (60 °C, for 1 h) followed by 60 mM Iodoacetamide (Sigma) (at room temperature in the dark for 45 min), then washed and dehydrated and incubated with 12.5 ng/ μ l trypsin (Promega, Grade IV) for 45 min. After the incubation the supernatant was replaced with 100 mM ammonium bicarbonate and the digestion was allowed to proceed overnight at 4 °C. Gel samples were washed with acetonitrile and 100 mM ammonium bicarbonate, treated three times each and the supernatant containing the digested peptides was collected

after each wash. Supernatants containing the tryptic peptides were concentrated in a speed vacuum unit. Tryptic peptides were resuspended in 30 μ l of 0.1 % acetic acid and loaded on a 10 cm (bed length) self-packed C18 (YMC-Waters 10 μ m) capillary pre-column (360 μ m o.d. x 100 μ m i.d.). After a 10 min rinse with 0.1 % acetic acid, the pre-column was connected to a 10 cm (bed length) self-packed 5 μ m C18 (YMC-Waters ODS- AQ) analytical capillary column (360 μ m o.d. x 50 μ m i.d.) with an integrated electrospray tip (less than 1 μ m orifice). Peptides were eluted with a 120 min gradient with solvents A (1 % acetic acid in SQ water) and B (90 % MeCN in 1 % acetic acid in SQ water): 10 min from 0 % to 15 % and 110 min from 15 % to 100 %, then directly electrosprayed into a quadrupole time of flight (QqTOF) mass spectrometer (QSTAR Elite, Applied Biosystems). The instrument was run in positive ion mode and MS/MS spectra of the five most intense peaks (exceeding 50-70 counts) with two to five positive charge states in the full MS scan were automatically acquired in information-dependent acquisition, target ions were excluded from further fragmentation for 50 to 60 seconds. The MS/MS accumulation was automatic, the fragment intensity multiplier set between 6 and 7 and the maximum accumulation was 3 seconds. MS/MS spectra were extracted and searched using Mascot version 2.1 (Matrix Science). Data was searched against the Swissprot human non- redundant protein database with trypsin specificity, allowing a maximum of two missed cleavages, with set mass tolerance of 2.2 Da for the precursor ion and 0.15 Da for the fragment ion. Data was search with fixed modification of carbamidomethyl (C) and variable modification of oxidation (M).

Mass spectrometry data analysis. Raw mass spec data were analysed using Mascot version 2.1 (Matrix Science, (<http://www.matrixscience.com>) followed by Scaffold 3 (Proteome Software). In order to be considered as hit, proteins had to score with a probability assigned by Scaffold of greater than 95 % and have at least two peptides identified that were

assigned greater than 90 % probability of being correctly identified from the spectra. Protein lists identified in GST and GST-RB1^N sample were compiled and proteins that qualified as hits in corresponding GST preparations were eliminated from the corresponding RB1^N list. In order to generate a consolidated list of candidate binding proteins, the candidate proteins had to be present in two or more independent RB1^N replicate runs. To further confirm the identity of peptides, manual sequencing the fragmentation spectra for selected candidates were performed.

Gene ontology analysis. DAVID functional annotation tool (<http://david.abcc.ncifcrf.gov>, Dennis et al., 2003) was used to identify gene ontologies enriched over a self-generated nuclear protein background database. To generate the background list, the entire proteome (obtained from Swissprot) was uploaded as a list to DAVID using Uniprot Accession Numbers and proteins classified as nuclear using GOTERM_CC_FAT were collated. The list of interacting proteins was uploaded to DAVID using Swissprot identifiers and compared to this background using GOTERM_BP_FAT. Gene ontologies that show ten-fold or greater enrichment over backgrounds and contained three or more protein hits were considered enriched.

Mammalian cell extract preparation. Cell nuclear extracts were prepared for GST affinity purification experiments. MCF-7 and HCT116 nuclear extract was generated from log phase cells. Cell monolayers were washed with PBS and nuclei generated by re-suspending them into 10 mM Tris pH 7.5, 10 mM KCl, 1.5 mM MgCl₂, 0.1 mM TCEP and 0.5 % Triton (1 x 10⁶ cells in 100 µl, at 4 °C). Suspensions were gently homogenized using a loose fitting pestle and nuclei sedimented (10,000 g for 20 min). HeLa nuclei (Cilibiotech) were

purchased from Cilibiotech. For extraction, nuclei were resuspended in three volumes of 30 mM Tris pH 7.5, 2.5 % Glycerol, 0.4 M NaCl, 1 mM MnCl₂, 2 mM TCEP, 2 mM Na₃VO₄, 10 mM NaF, containing DNase 1 (50 U/ml) and RNase A (14 U/ml) with 1 complete protease tablet (Roche) per 50 ml, and homogenised using a loose fitting pestle. After 20 min incubation on ice, the debris was sedimented by centrifugation at 20,000 g for 30 min at 4 °C and supernatants decanted. For large scale purifications nuclear supernatants were dialysed against binding buffer (30 mM Tris pH 7.5, 2.5 % Glycerol, 80 mM NaCl, 0.1 mM EDTA, 0.1 mM TCEP). Any precipitates were removed by centrifugation (20,000 g for 1 h). Extracts were precleared by incubation with Glutathione Sepharose 4 Fast Flow bound GST (2 mg of GST for 2.5 x 10⁹ nuclei) overnight at 4 °C. The resin-bound GST was removed by centrifugation (1000 g for 5 min) and the supernatant collected. Protein concentrations in precleared lysates were estimated by DC Protein Assay (Bio-Rad). For small-scale affinity purification nuclear extracts were diluted three fold in binding buffer. To generate total cell lysates for immunoblotting cell monolayers were washed with PBS followed by extraction buffer (50 mM Tris pH 7.4, 250 mM NaCl, 1 mM DTT, 1 mM EDTA, 1 mM NaF, 10 mM β-glycerophosphate, 0.1 mM NaVO₄ plus Roche complete proteinase inhibitors) without Triton-100, then scraped into extraction buffer containing 0.2 % Triton X-100, and incubated on ice for 10 min. Extracts for the analysis of NHEJ components were generated by adding SDS loading buffer directly to these lysates. Lysates were spun through glass wool plugs to remove nucleic acid. For immunodetection of RB1, lysates were centrifuged at 10,000 g for 20 min to remove insoluble material.

GST affinity purification. Large-scale purifications used 2 mg of purified GST RB^N or GST protein bound to 200 μl Glutathione Sepharose 4 Fast Flow resin which was incubated with 0.7 mg pre-cleared HeLa nuclear extract for 2 h with 4 °C. Following incubation resins were

washed three times with binding buffer (30 mM Tris pH 7.5, 2.5 % Glycerol, 80 mM NaCl, 0.1 mM EDTA, 0.1 mM TCEP) and once with binding buffer containing 150 mM NaCl. Associated proteins were eluted with binding buffer containing 1 M NaCl. Affinity purified materials were fractionated on a 12 % Bis-Tris gel (Invitrogen). For small scale affinity purification 400 µl of MCF-7 or HCT116 extract was incubated with 400 µg Glutathione Sepharose 4 Fast Flow bound GST-RB^N or GST and bound to for 2 h at 4 °C. Associated proteins were eluted with 4 x SDS protein loading buffer and analysed by immunoblotting.

Co-immunoprecipitation. Cell nuclei were prepared as for GST affinity purification. Nuclear proteins were extracted in 0.32 M sucrose, 50 mM Tris (pH 7.5), 4 mM MgCl₂, 1 mM CaCl₂, 0.1 mM AEBSF containing 10 U per 2 x 10⁶ cells micrococcal nuclease (New England Biolabs), with digestion for three hours at room temperature, supernatants were collected and residual soluble material extracted from the insoluble fraction using 1 mM Tris-HCl (pH 7.4), 10 mM EDTA, 1 mM AEBSF, 0.32 mM sucrose and 150 mM NaCl. RB1 was immunoprecipitated from this extract using rabbit serum against a human RB1 C-terminal fragment (aa 763-928) (Zarkowska and Mitnacht, 1997) crosslinked Protein A/G PlusTM Agarose (Thermo Fisher). Immunoprecipitates were washed and precipitated proteins eluted according to the manufacturer's instructions. Eluted proteins were subjected to immunoblotting.

Proximity ligation assay. Proximity ligation assays were performed using Duolink technology (Cambridge Biosciences) in accordance with the manufacturer's recommendations. Cells were grown on eight well µ-slides imaging slides (Ibidi). Where

applicable cells were reverse transfected with siRNA using HiPerFect lipid transfection reagent (Qiagen) with a fixed siRNA concentration of 20 nM prior to seeding onto Ibidi μ -slides. Cells were exposed to 500 nM PD0332991 for 18 h where indicated and subjected to 5 Gy irradiation or mock irradiated where indicated. Cells were fixed with 4 % w/v formalin (Sigma) for 20 min at room temperature, reacted with mouse anti-RB1 (BD Pharmingen) in combination with goat anti-XRCC6 (raised in goat, Santa Cruz), all at a dilution of 1:250, overnight at 4 °C. Proximity of primary antibody reactivity was detected by PLA probes (MINUS Goat and PLUS Mouse) followed by a ligation and amplification reaction as described in the manufacturer's instructions. Slides were imaged using a Nikon Confocal microscope. Controls were carried out to ensure the signals were protein and interaction selective. The Cell profiler was used for signal quantification using the example speckle counting pipeline. For immunofluorescence staining parallel specimen were permeabilised with 1 % Triton X-100 in Tris buffered salt (TBS) and blocked with blocking buffer (5 % Milk powder in TBS with 1 % Tween). Immunostaining was performed as for the detection of γ H2AX.

Cells, cell culture and cell synchronisation. HeLa cell nuclei were purchases from CIL BIOTECH s.a. HCT116, MCF-7, U2OS, SAOS-2 cells were purchased from American Type Culture Collection (ATCC). Wild type and congenic RB1^{-/-} primary mouse embryonic fibroblasts (MEFs) were derived from individual day 13.5 embryos as previously described (Alani et al., 2001). TKO MEFs were provided by Professor H Te Riele, Netherlands Cancer Institute (Dannenberget al., 2000). All MEFs had 129/Ola background. The CDK4/6 selective inhibitor PD0332991 (Fry et al., 2004) was obtained from Axon. In order to study cell cycle checkpoint regulation, nocodazole was used to induce a cell cycle

arrest in transfected TKO MEFs. Cells were treated with 0.5 $\mu\text{g/ml}$ nocodazole (Sigma, www.sigmaaldrich.com) for 24 h prior to harvest. NU7441 (Tocris) was used as an inhibitor of PRKDC, a protein required for classic NHEJ (Zhao et al., 2006). Cells were treated with 5 μM NU7441 24 h prior to 5 Gy irradiation or for the duration of the NHEJ reporter assay. MCF-7 and HCT116 cells were synchronised in the G1, S or G2/M phases of the cell cycle. G1 enriched HCT116 and MCF7 cells were generated by treatment with 400 nM PD 033299 for 17 h (HCT116) or 19 h (MCF-7). S phase and G2/M cells underwent a double thymidine block (2 μM) followed by release into nocodazole (100 nM). MCF-7 cells were harvested 3 h (S phase enriched) or 10 h later (G2/M phase enriched). HCT116 cells were harvested 2 h (S phase enriched) or 8 h (G2/M phase enriched) after release into nocodazole. Cell cycle distributions were assessed using propidium iodide staining and flow cytometry. Ser780 phosphorylation on RB1, representing as surrogate biomarker for active CDK4/6 was assessed using immunoblotting. DNAPK inhibitor Nu7026 was used at a final concentration of 10 μM . Inhibitors were added 1 h prior to irradiation and remained present throughout the remainder of the experiment.

Cell irradiation. Irradiation of cells was performed using an AGO HS 320/260 electrical source Xray set, with a dose rate of 5 Gy/min. Irradiation was conducted at room temperature except for Comet analysis where cells were placed on ice prior to irradiation. Following irradiation cells were immediately returned to a humidified incubator at 37 $^{\circ}\text{C}$ with 5 % CO_2 .

Analysis of Chromosomal radiosensitivity. Cells were plated in 6-well dishes such that they were no more than 50 % confluent at the time of harvest. Cells transfected with siRNA were used 48 h post-transfection. Cells were detached using warm trypsin solution, trypsin

was neutralised with an equal volume warm culture medium and cells sedimented by centrifugation at 800 rpm for 5 mins. The supernatants were removed and cells resuspended in 1 ml of warm medium. 5 ml of warm 0.4 % KCl were added and cells incubated for 15- 30 min at 37 °C. Three drops of fixative solution [methanol-acetic acid (3:1)] were added and cells were sedimented at 800 g for 8 min. The supernatant was removed and 5 ml of fixative was added drop-wise. Centrifugation and fixative addition was repeated two more times. Fixed cells were stored at -20 °C until analysis. Chromosome-type (dicentrics, centric rings and excess acentric fragments, i.e. those not associated with dicentrics) and chromatid-type aberrations (chromatid gaps, breaks and exchanges) were scored by eye at 1000x magnification under oil immersion using the Metafer® metaphase finding system (Zeiss, UK).

Comet analysis. Cells were plated in 6-well plates (1×10^5 cells/well). Wherever required cells were transfected with siRNA for 48 h prior to irradiation. At the time required irradiated cells were harvested using trypsin, resuspended in fetal calf serum containing 10 % DMSO and stored at -80 °C until analysis. COMET single cell gel electrophoresis (comet) assay was performed as described in (Spanswick et al., 2010). Immediately before analysis cells were thawed on ice and diluted in cold serum-free DMEM to give a final concentration of 2.5×10^4 cells/ml. All procedures were carried out in subdued lighting. 0.5 ml of the appropriate cell suspension (i.e. 1.25×10^4 cells) was mixed with 1 ml of melted 1 % low gelling temperature (LGT)-agarose in water then placed onto the centre of a microscopic slide pre-coated with 1 % type 1-A agarose in water. Duplicate replicates were generated for each condition. Cells were lysed by immersion of the slides for 1 h in alkaline lysis buffer (100 mM disodium EDTA, 2.5 M NaCl, 10 mM Tris-HCl pH 10.5) containing 1 % Triton X-100. Slides were washed every 15 min in distilled water for 1 h. Slides were then incubated in alkali buffer (50

mM NaOH, 1 mM disodium EDTA, pH 12.5) for 45 min followed by electrophoresis in the same buffer for 25 min at 18 V (0.6 V/cm), 250 mA. The slides were finally rinsed in neutralising buffer (0.5 M Tris-HCl, pH 7.5) and then saline. After drying, the slides were stained with propidium iodide (2.5 µg/mL) for 30 min then rinsed in distilled water. Images were visualised using a NIKON inverted microscope with high-pressure mercury light source, 510-560 nm excitation filter and 590 nm barrier filter at x20 magnification. Images were captured by an on-line CCD camera and analysed using Komet Analysis software 6.0 (Andor Technology, U.K.). For each duplicate slide 25 cells were analysed. The tail moment for each image was calculated as the product of the percentage DNA in the comet tail and the distance between the means of the head and tail distributions (Olive et al., 1990).

DNA Constructs. pGEX6p1 expressing human RB1 40-355, human RB1 40-355^{Poly G} and RB 40-355²⁴⁰⁻²⁴² are described in (Hassler et al., 2007). pGex6P1 expressing RBL1 19-330 and RBL2 24-418 were generated by cloning a PCR generated coding sequence in frame into the BamHI site of pGEX6p1. NHEJ reporter plasmids pim-EJ5-GFP and pCBAI-SceI are described in (Bennardo et al., 2008). pDsRed was obtained from Clontech. Plasmids pcDNA3 9E10 and pcDNA3 9E10 RB1, -3xWT-luc pCMV-E2F1 and pCMV-DP1 are described in (Chew et al., 1998), pcDNA3-9E10 RB1^{PolyG} and pcDNA3-9E10 RB1²⁴⁰⁻²⁴² was cloned by overlap extension polymerase chain reaction with primers: 5'-cgggatccatgccgcccaaaacc-3'; 5'-gacgagaggcaggtcctc-3'; and 5'-gaggacctgcctctcgtc-3'; 5'-gcggatccttatctctgtgtttcaaaactg-3' using pGEX6P1 RB1 40-355^{PolyG} or pGEX6P1 40-355 240-242 and pcDNA9E10 RB1 as templates, followed by insertion of the into pcDNA3-9E10 RB1 using BamHI and EcoRI sites.

Antibodies. Antibodies used for immunoblotting and immunostaining were mouse anti-XRCC5 (AB3107, Abcam), mouse anti-XRCC6 (MS-329, Thermo), mouse anti-RB1 (G3-245, BD biosciences), mouse anti-DsRed (E64-1077, BD biosciences), anti-RB1-PS780 rabbit monoclonal antibody (E182 , Epitomics), mouse anti-MYC tag (4A6, Upstate), rabbit anti-EGFP (26-39, Novagen), anti-mouse anti-alpha-tubulin (B-5-1-2, Invitrogen), anti-PRKDC-PS2056 (EPR5670, Abcam) and anti-PRKDC (3H6, Thermo). In house rabbit serum raised against a C-terminal human RB1 fragment (aa 763-928) was used for co-immunoprecipitation experiments. Rabbit anti-mouse IgG (M7023, Sigma) was used as an irrelevant control serum. Mouse anti-phospho γ H2AX was purchased from Millipore (05-636), secondary antibodies 488 Alexa Fluor-conjugated anti-mouse IgG (A-110001, Invitrogen), 647 Alexa Fluor-conjugated anti-mouse IgG (A21236, Invitrogen) and 647 Alexa Fluor-conjugated anti-goat IgG (A21447, Invitrogen) were purchased from Invitrogen. Goat anti- XRCC6 (sc-1487, Santa Cruz) anti-RB1 (G3-245, BD biosciences) were used for PLA.

siRNAs and transfection. RB1 specific siRNA sequence GGUUCAACUACGCGUGUAAAdTdT was from Dharmacon. RBL1 siRNA pool (M-003298-02, siGenome SMART pool) and RBL2 siRNA pool (M-003299-03, siGenome SMART pool) and LIG4 siRNA pool (M-004254-04, siGenome SMART pool) was purchased from Dharmacon. Non-targeting AllStars Negative Control siRNA, was obtained from Qiagen. siRNA transfections were performed using lipofectamineTM (Life Technologies) according to the manufacturer's instructions using fixed total siRNA concentration of 20 nM.

Cell based assays for assessment of RB1 function. For G1 arrest assays SAOS-2 cells were electroporated with 0.2 µg pCMV-CD20, 1.6 µg pcDNA3-9E10 RB1 wild type or variant. Electroporation was carried out using Cell Line Nucleofector® Kit V (Lonza) according to manufacturer's instructions. Electroporated cells were seeded and 24 h later treated with 0.6 µg/ml nocodazole (Sigma) to distinguish cycling cells in G1 from cells arrested in G1. 24 h later non-adherent and adherent cells were collected in PBS/EDTA, washed with PBS, resuspended in PBS containing 5 µl FITC-conjugated anti-CD20 antibody (BD Pharmingen) and incubated at 4 °C for 30 min. Cells were washed with PBS and fixed in 70 % ethanol for 30 min at 4 °C. After fixation, PI stain was used to determine the percentage of cells in each cell cycle phase. To assess RB mediated reduction of colony outgrowth SAOS-2 cells were transfected with 1.6 µg pcDNA3-9E10 RB1 wild type or variant, 0.15 µg pBABE-puromycin, 0.1 µg RSV-β-galactosidase and 0.1 µg EGFP using electroporation as for G1 arrest analysis. 400 µl of the electroporated cell suspension was seeded into two 10 cm petri dishes in media containing 0.6 µg/ml puromycin to select for transfected cells. Colonies were counted after 14 days and normalised for β-galactosidase activity. The amount of colonies for the empty vector was set at 100 %. The remaining cells were grown for 36 h and harvested to quantify β-galactosidase activity and for monitoring RB1 transgene expression by immunoblotting. The GalactoLight β-Galactosidase Reporter Gene Assay System (Applied Biosystems) was used to quantify β-galactosidase activity, EGFP was immunoblotted alongside RB1 as an additional loading control. To assess E2F repression SAOS-2 cells were transfected with 0.1 µg pGL2-3xWT-luc, 0.01 µg pCMV-E2F1, 0.02 µg pCMV-DP1, 0.45 µg pcDNA3-9E10 RB1 wild type or variant, 0.1 µg RSV-β-galactosidase and 0.1 µg EGFP using electroporation as for G1 arrest analysis. The reporter construct contains an artificial promoter with three E2F binding sites connected to a luciferase reporter gene. Luciferase activity was determined after 40 h using the Luciferase Assay System (Promega) according to

manufacturer's instructions using a luminometer with an injector. Luciferase values were normalised to β -galactosidase activity.

REFERENCES

Alani, R.M., Young, A.Z., and Shifflett, C.B. (2001). Id1 regulation of cellular senescence through transcriptional repression of p16/Ink4a. *Proceedings of the National Academy of Sciences of the United States of America* *98*, 7812-7816.

Bennardo, N., Cheng, A., Huang, N., and Stark, J.M. (2008). Alternative-NHEJ is a mechanistically distinct pathway of mammalian chromosome break repair. *PLoS genetics* *4*, e1000110.

Chew, Y.P., Ellis, M., Wilkie, S., and Mittnacht, S. (1998). pRB phosphorylation mutants reveal role of pRB in regulating S phase completion by a mechanism independent of E2F. *Oncogene* *17*, 2177-2186.

Dannenbergh, J.H., van Rossum, A., Schuijff, L., and te Riele, H. (2000). Ablation of the retinoblastoma gene family deregulates G(1) control causing immortalization and increased cell turnover under growth-restricting conditions. *Genes & development* *14*, 3051-3064.

Fry, D.W., Harvey, P.J., Keller, P.R., Elliott, W.L., Meade, M., Trachet, E., Albassam, M., Zheng, X., Leopold, W.R., Pryer, N.K., *et al.* (2004). Specific inhibition of cyclin-dependent kinase 4/6 by PD 0332991 and associated antitumor activity in human tumor xenografts. *Molecular cancer therapeutics* *3*, 1427-1438.

Hassler, M., Singh, S., Yue, W.W., Luczynski, M., Lakbir, R., Sanchez-Sanchez, F., Bader, T., Pearl, L.H., and Mittnacht, S. (2007). Crystal structure of the retinoblastoma protein N domain provides insight into tumor suppression, ligand interaction, and holoprotein architecture. *Molecular cell* *28*, 371-385.

Olive, P.L., Banath, J.P., and Durand, R.E. (1990). Heterogeneity in radiation-induced DNA damage and repair in tumor and normal cells measured using the "comet" assay. *Radiation research* 122, 86-94.

Spanswick, V.J., Hartley, J.M., and Hartley, J.A. (2010). Measurement of DNA interstrand crosslinking in individual cells using the Single Cell Gel Electrophoresis (Comet) assay. *Methods in molecular biology* 613, 267-282.

Zarkowska, T., and Mittnacht, S. (1997). Differential phosphorylation of the retinoblastoma protein by G1/S cyclin-dependent kinases. *J Biol Chem* 272, 12738-12746.

Zhao, Y., Thomas, H.D., Batey, M.A., Cowell, I.G., Richardson, C.J., Griffin, R.J., Calvert, A.H., Newell, D.R., Smith, G.C., and Curtin, N.J. (2006). Preclinical evaluation of a potent novel DNA-dependent protein kinase inhibitor NU7441. *Cancer research* 66, 5354-5362.